Economic Geology, v. 117, no. 8, pp. 1809–1825

Lithologic and Geochemical Constraints on the Genesis of a Newly Discovered Orebody in the Jinchuan Intrusion, NW China

Jian Kang,[1,2] Xie-Yan Song,[1,†] Ting-Mao Long,[1,2] Qing-Lin Liang,[1] Stephen J. Barnes,[3] Lie-Meng Chen,[1] De-Xian Li,[4] Qi-Xing Ai,[4] and Ya-Lin Gao[4]

[1]*State Key Laboratory of Ore Deposit Geochemistry, Institute of Geochemistry, Chinese Academy of Sciences, Guiyang 550081, P. R. China*

[2]*University of Chinese Academy of Sciences, Beijing 100049, P. R. China*

[3]*Commonwealth Scientific and Industrial Research Organisation (CSIRO) Mineral Resources, Kensington, Perth, Western Australia 6151, Australia*

[4]*Jinchuan Group Ltd., Jinchuan, Gansu 737100, P. R. China*

Abstract

The Jinchuan Ni-Cu-platinum group element (PGE) sulfide deposit is one of the world's major magmatic sulfide deposits. The Jinchuan intrusion originally consists of two independent bodies, named the Western and Eastern intrusions. Recently, an underground exploration program discovered a large economic orebody in the Fine-Grained unit of the Western intrusion, independent of the orebody No. 24 that occurs at the base of the Coarse-Grained unit. The newly discovered orebody dips to the southwest with thicknesses of 20 to 150 m and is composed of olivine-sulfide cumulates with net-textured sulfide overlain by lherzolite with disseminated sulfide. The net-textured olivine-sulfide cumulates have average grades of 2.1 wt % Ni and 1.2 wt % Cu, whereas the disseminated ores in the lherzolite have average grades of 0.6 wt % Ni and 0.4 wt % Cu. This makes this orebody, named orebody No. 3 and hosted in segment III, the fourth largest at Jinchuan. The sharp lithologic and chemical variation between the net-textured olivine-sulfide cumulates and the disseminated sulfide-bearing lherzolite indicates that they were formed by different processes. Evident differences in sulfide-free whole-rock compositions reflect the dunite forming as olivine adcumulate and the lherzolite as olivine orthocumulate with variable trapped liquid abundances. The olivine-sulfide cumulates were formed by percolation of sulfide liquid into the olivine adcumulates, expelling the interstitial silicate melts upward, whereas the disseminated ores in the lherzolite were formed by settling of finely dispersed sulfide droplets in the olivine crystal mush, within which pyroxene crystallized from the interstitial melts. Variations of PGE tenors of the net-textured sulfides demonstrate fractionation of the sulfide liquids. The relatively high PGE tenors of the disseminated sulfides compared with the net-textured sulfides are associated with upgrading of the sulfides due to reaction with fresh magma.

Introduction

The Jinchuan Ni-Cu-platinum group element (PGE) sulfide deposit in Northwest China (Fig. 1a) is one of the world's most valuable magmatic sulfide deposits and contains ~620 million metric tons (Mt) of sulfide ores with average grades of 1.1 wt % Ni and 0.7 wt % Cu in the premining resource (latest data from reserve verification report of Jinchuan Group Ltd., 2017). Previous studies have concluded that the Jinchuan deposit was formed by segregation and concentration of sulfides from high-Mg basaltic magma in a dynamic magma conduit system (Chai and Naldrett, 1992a; Li et al., 2004; Song et al., 2009, 2012; Tonnelier, 2010; Chen et al., 2013; Duan et al., 2016; Mao et al., 2018a). The distinct lithologic and geochemical characteristics of the orebodies No. 1 and No. 2 in segment II and the orebody No. 24 in segment I indicate that they were formed by different processes (Fig. 2) (de Waal et al., 2004; Li et al., 2004; Song et al., 2009; Chen et al., 2013). However, only subeconomic sulfide mineralization (0.5 wt % Ni and 0.3 wt % Cu) was discovered in the 1960s prospecting programs in segment III (Sixth Geological Unit, 1984; Chen et al., 2013).

In 2017 to 2018, a layer of net-textured sulfide ores containing up to ~2.1 wt % Ni and ~1.2 wt % Cu was discovered at the base of segment III via an underground exploration program (Fig. 2d). The new discovered net-textured ore layer is >400 m long with thicknesses up to 60 m, dips to the southwest, and is open at depth (Fig. 2d), making the orebody in segment III the fourth largest orebody at Jinchuan. In this paper, it is named orebody No. 3, which contains more than 3×10^7 t sulfide ores with average grade of ~1.2 wt % Ni and ~0.6 wt % Cu according to the current drill cores. In this study, the lithologic and geochemical features of segment III and orebody No. 3 are investigated and described. Processes of sulfide segregation, migration, and deposition in a dynamic conduit system are discussed on the basis of PGE and semimetal element data of the sulfide ores.

Geologic Background

The Jinchuan Ni-Cu sulfide deposit is located in the northern margin of the Longshoushan terrane, which constitutes the southwestern boundary of the North China craton (Fig. 1a). Geologic background and field relationships of the Jinchuan deposit have been extensively described (Chai and Naldrett, 1992b; Tang and Li, 1995; Song et al., 2006, and references therein; Lehmann et al., 2007; Tang et al., 2009;) and only a brief introduction is given in this study. The NW-SE–trending Jinchuan intrusion is divided by NE-trending strike-slip faults into four segments: III, I, II, and IV from west to east (Fig. 2a; Sixth Geological Unit, 1984; Song et al., 2012). The country rocks of the intrusion are Paleo-Mesoproterozoic

†Corresponding author: e-mail, songxieyan@vip.gyig.ac.cn

ISSN 0361-0128; doi:10.5382/econgeo.4911; 17 p.
Digital appendices are available in the online Supplements section.

Submitted: April 7, 2021/Accepted: August 23, 2021

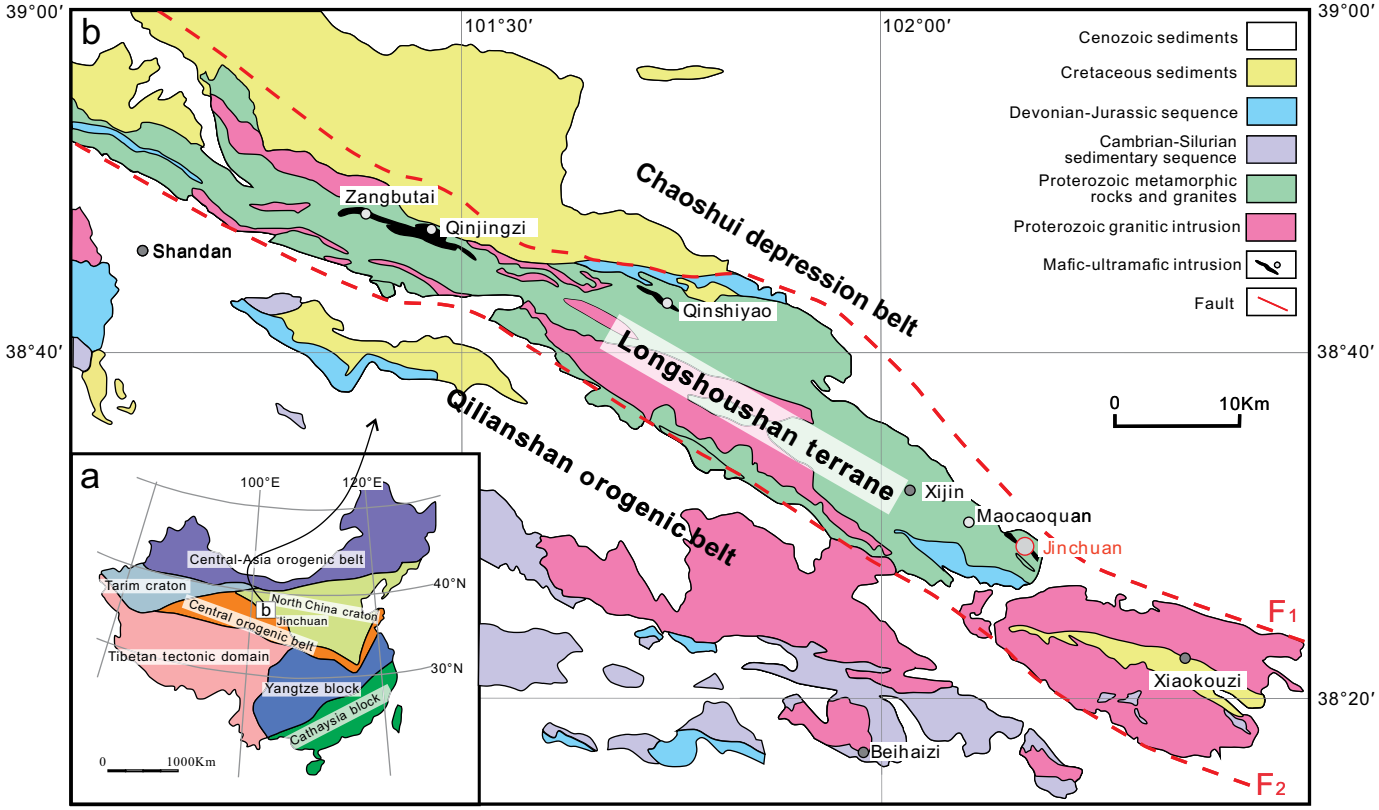

Fig. 1. Tectonic sketch map of China (a) and geologic map of the Longshoushan terrane, showing the location of the Jinchuan deposit (b) (modified after Song et al., 2009, 2012; Chen et al., 2013).

metamorphic gneisses, schists, marbles, and granites. Based on petrologic features of the segments and the nature of the faults, Song et al. (2012) proposed that there were two independent intrusions, one on either side of the fault $F_{16\text{-}1}$. Segments I and III make up the Western intrusion and segments II and IV constitute the Eastern intrusion (Fig. 2a).

Lithology of Segment III

The Western intrusion has two lithologic cycles and was broken by the fault F_8 into segment III in the west and segment I in the east (Fig. 2b). Both of these segments comprise dunite, lherzolite, and pyroxenite from the base to the top as olivine mode decreases and pyroxene mode increases gradually upward. Grain sizes of olivine in the two cycles are remarkably different (Song et al., 2012; Chen et al., 2013). The grain diameter of olivine in the upper-cycle rocks ranges from 0.5 to 3 mm and in the lower-cycle rocks varies from 6 to 10 mm. Thus, the upper and lower cycles were named the Fine-Grained and Coarse-Grained units in this study to highlight the distinct lithologic features. The sharp contact between the dunite at the bottom of the Fine-Grained unit and the lherzolite at the top of the Coarse-Grained unit indicates two cycles of magma emplacement (Fig. 2b). Observations of drill holes demonstrate that the Fine-Grained and Coarse-Grained units predominantly occur in the western and eastern portions of the Western intrusion, respectively. Thus, segments III and I are mainly composed of the Fine-Grained and Coarse-Grained units, respectively (Fig. 2d; Song et al., 2012; Chen et al., 2013).

Segment III is covered by 40 to 50 m of Quaternary sediments. Drill holes reveal that it is ~500 m long, trends northwest-southeast, and dips 60° to 70° to the southwest (Fig. 2c). It becomes thinner toward the west and has undulating top and bottom surfaces (Fig. 2c, d). In segment III, the fine-grained olivine-sulfide cumulates, up to 60 m thick, are overlain by 50- to 300-m-thick fine-grained lherzolite as olivine decreases and pyroxene increases (Fig. 2d). The base of the Fine-Grained unit consists of olivine-pyroxenite with variable thicknesses when in direct contact with metamorphic wall rocks in segment III (Fig. 2d). The olivine-pyroxenite is absent at the base of Fine-Grained unit when it overlies the Coarse-Grained unit in segment I (Fig. 2b). A few interlayers

Fig. 2. (a) Distribution of Eastern and Western intrusions, ultramafic segments, and faults at Jinchuan. (b) Simplified sketch of the Western intrusion, which was divided into segments I and III by the fault F_8 (modified after Song et al., 2012). (c) Geologic map of segment III at the level of ~100 m beneath the surface. Drill hole line I-24 across segment I shows that the fine-grained dunite at the bottom of the Upper unit is sharply contacted with the coarse-grained lherzolite at the top of the Lower unit of the Western intrusion. Drill hole line II-14 across segment II shows a concentric structure of Eastern intrusion. (d) Simplified horizontal sections at elevations of 1,430, 1,300, and 1,200 m, as well as the drill hole lines of III-5, III-8, and III-11 (data from exploration report of segment III of Jinchuan Group Ltd., 2020).

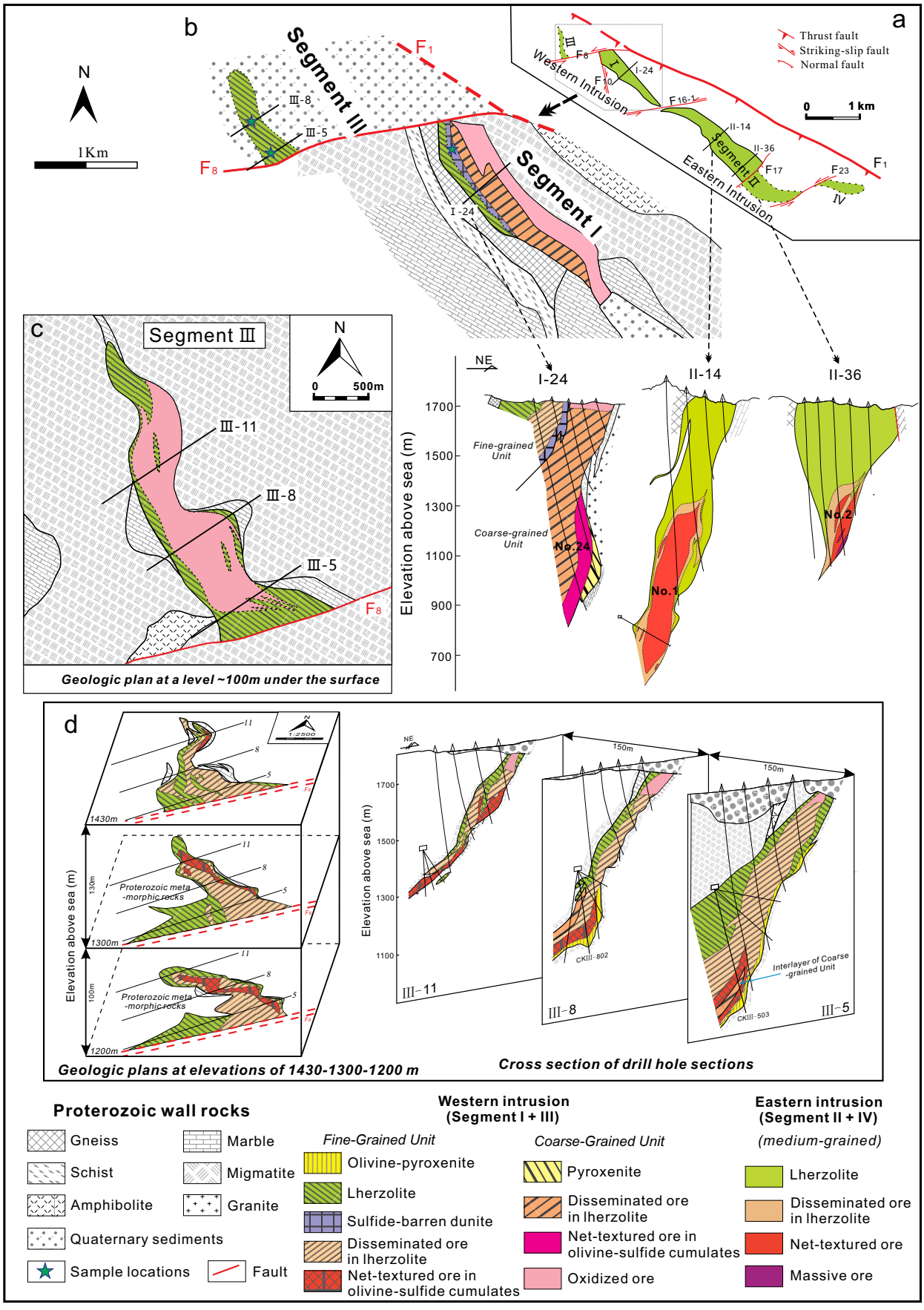

of coarse-grained lherzolite are embedded in the olivine-sulfide cumulates or lherzolite of the Fine-Grained unit (Fig. 2d). The sharp contacts and very large differences in olivine grain sizes and modes of rock-forming minerals and sulfides between the coarse-grained lherzolite and the fine-grained olivine-sulfide cumulates or lherzolite cannot be explained by fractionation of a uniform magma (Fig. 2d). Song et al. (2012) proposed that the Coarse-Grained unit was emplaced slightly later than the Fine-Grained unit.

In segment III, the fine-grained olivine-sulfide cumulates consist of 65 to 80% olivine and 20 to 35% sulfide as net-textured ores. The fine-grained lherzolite consists of 45 to 75% olivine and 20 to 40% pyroxene and can contain up to 15% sulfides as disseminated ores. The coarse-grained lherzolite interlayer consists of 40 to 60% olivine, 25 to 45% pyroxene, and 5 to 15% sulfide (Fig. 2d). In these rocks, olivine experienced serpentinization and pyroxene was altered to chlorite and tremolite (App. Fig. A1).

Characteristics of Orebody No. 3

As shown in Figures 2 and 3, orebody No. 3 consists of net-textured olivine-sulfide cumulates overlain by disseminated sulfidic fine-grained lherzolite. The net-textured ore layer is up to 60 m thick and extends downward for 1,100 to 1,400 m, whereas the disseminated ore layer is 30 to 150 m thick and extends downward for 1,100 to 1,600 m (Fig. 2d). Both the disseminated and net-textured ore layers become thicker toward the east; therefore, orebody No. 3 possibly extends into the Fine-Grained unit of segment I. The net-textured olivine-sulfide cumulates contain 20 to 35 vol % sulfides (Fig. 4). The dominant sulfides are pyrrhotite (10–30 modal %), pentlandite (4–10 modal %), and chalcopyrite (1–4 modal %), and fine-grained olivines are completely enclosed by the sulfides (App. Figs. A1e, A2b). In contrast, sulfide contents in the above disseminated sulfide ore layer decrease abruptly to less than 10 vol % (Fig. 4). The disseminated ores have interstitial disseminated texture in the terminology of Barnes et al. (2017a) and contain 1 to 8% pyrrhotite, 1 to 5% pentlandite, and 1 to 3% chalcopyrite (App. Figs. A1c, d, A2a). The fine-grained olivine-pyroxenite underneath the net-textured ore layer contains up to 15% sulfides (Fig. 2d). Cubanite lamellae occur in some grains of chalcopyrite (App. Fig. A2c). The proportion of olivine to pyroxene is about 90:10 in the fine-grained olivine-sulfide cumulates (net-textured ores) to 50–80:20–50 in the fine-grained lherzolites (disseminated ores) (Fig. 3a-2, b-2). Magnetite, resulting from hydrothermal alteration, occurs as very fine networks in the altered olivine or as fine veins at the boundaries of the sulfides (App. Figs. A1, A2). The hydrothermal alteration also produced fine anhedral pyrite at margins of the sulfides (App. Fig. A2c, d).

The two layers of coarse-grained lherzolite embedded within the net-textured fine-grained olivine-sulfide cumulates or above the fine-grained lherzolite contain disseminated sulfides (Figs. 2d, 3). In particular, the coarse-grained lherzolite interlayer contains 10 to 15 vol % sulfides (up to 20%), which is visibly lower than the overlying and underlying fine-grained olivine-sulfide cumulates (Fig. 4a).

Mineral Composition and Petrogeochemistry

Thirty-eight samples of ultramafic rocks and sulfide ores were collected from two boreholes, CKIII-503 and CKIII-802, in segment III (Fig. 2d). In addition, three fine-grained sulfide-barren dunites (containing sulfides less than 8 vol %) were collected in the open pit of segment I (Fig. 2b). Compositions of olivine and whole rock have been measured in this study. The analytical methods are described in Appendix Methods.

Olivine compositions

The olivine from the fine-grained olivine-sulfide cumulates and lherzolite in segment III have forsterite percentages (Fo = 79.0–84.9 mol %) and Ni contents (1,070–2,110 ppm) comparable with the olivine from the rocks in segments I and II (Fo = 76–85.5 mol % and Ni = 1,200–2,500 ppm) (App. Table A1) (Chai and Naldrett, 1992a; Li et al., 2004; Chen, 2009; Tonnelier, 2010). It is noteworthy that the olivine in the fine-grained lherzolite has larger variations in forsterite values (80.8–84.9 mol %) and Ni contents (1,150–2,110 ppm) than those in the underlying fine-grained olivine-sulfide cumulates (Fo = 81.7–83.9 mol %, Ni = 1,250–1,850 ppm) (Fig. 3). In contrast, the olivine in the coarse-grained lherzolite has relatively low forsterite values (80.0–82.1 mol %) and Ni contents (1,110–1,670 ppm) (Fig. 3a, b). Appendix Figure A3 shows a roughly negative correlation between forsterite and Ni for the olivine from the fine-grained olivine-sulfide cumulates and lherzolite and a positive correlation for the olivine from the coarse-grained lherzolite. It might be attributed to the reaction of the olivine with sulfide liquid and with silicate liquid, respectively (App. Fig. A3).

Whole-rock geochemistry

As listed in Appendix Table A2, most of the samples have large loss on ignition (LOI) values (3.5–13.4 wt %) because of alteration and high sulfide contents. Therefore, the concentrations of oxides and S have been recalculated to 100% on a volatile-free (anhydrous) basis before plotting the diagrams mentioned below.

Stratigraphic variations of the two drill holes illustrate that the fine-grained olivine-sulfide cumulates have the lowest contents of Al_2O_3 (0.72–1.89 wt %) and TiO_2 (0.06–0.17 wt %) and the highest contents of Fe_2O_{3T} (total Fe represented as Fe_2O_3) (20.9–33.1 wt %) (Fig. 3). The fine-grained lherzolite is relatively higher in MgO (30.5–35.0 wt %), Al_2O_3 (1.90–3.84 wt %), and TiO_2 (0.19–0.36 wt %) and lower in Fe_2O_{3T} (12.4–16.15 wt %) than the fine-grained olivine-sulfide cumulates. It is notable that Fe_2O_{3T} and MgO contents of the net-textured

Fig. 3. Stratigraphic variations of grain size, modal %, forsterite (Fo) percentage and Ni content (ppm) of olivine as well as whole-rock contents of MgO, Fe_2O_{3T}, Al_2O_3, CaO, and TiO_2 and Mg/Al ratio of the drill holes CKIII-503 (a) and CKIII-802 (b) through segment III. The Fine-Grained unit consists of fine-grained olivine-sulfide cumulates, lherzolite, and olivine-pyroxenite characterized by olivine grain sizes of 0.5 to 3 mm in diameter. Interlayers of the coarse-grained lherzolite containing olivine with diameters of 6 to 10 mm intruded into the Fine-Grained unit.

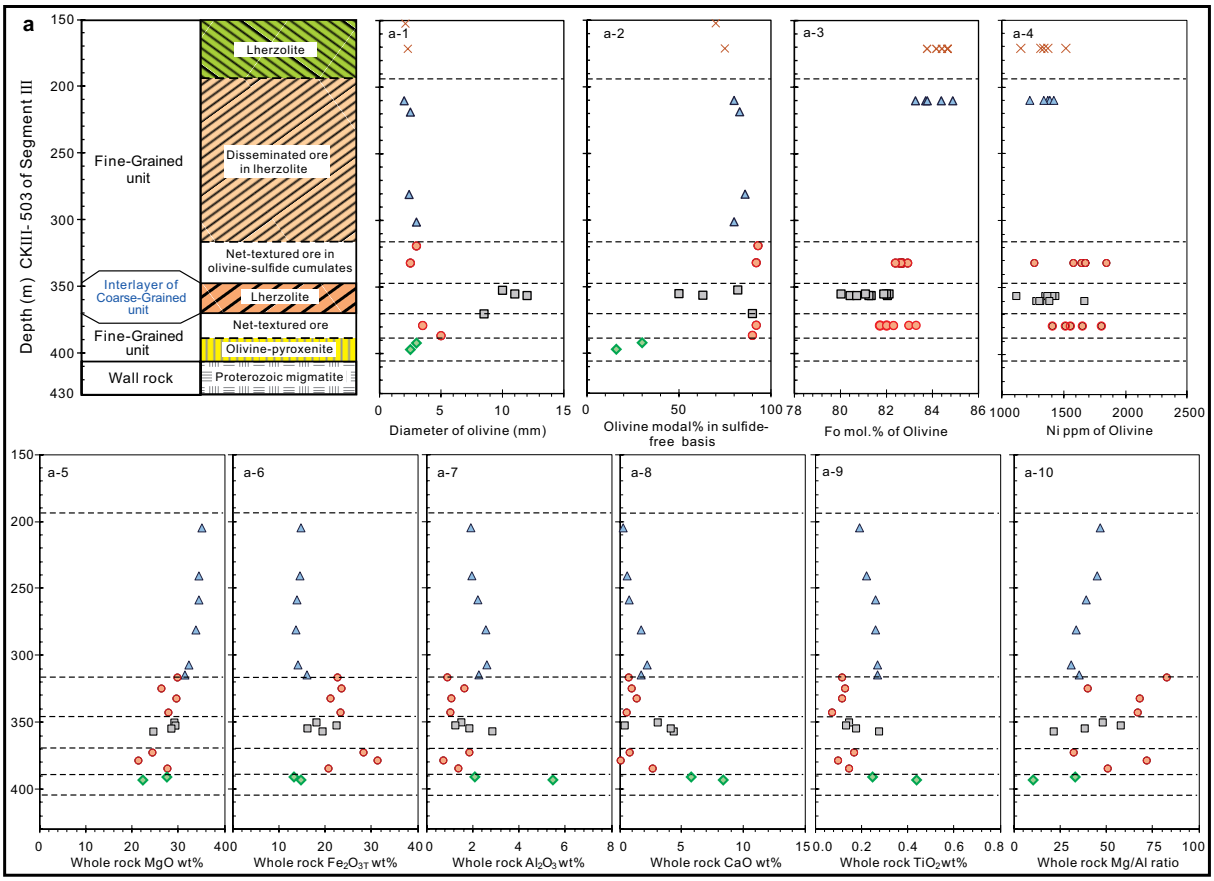

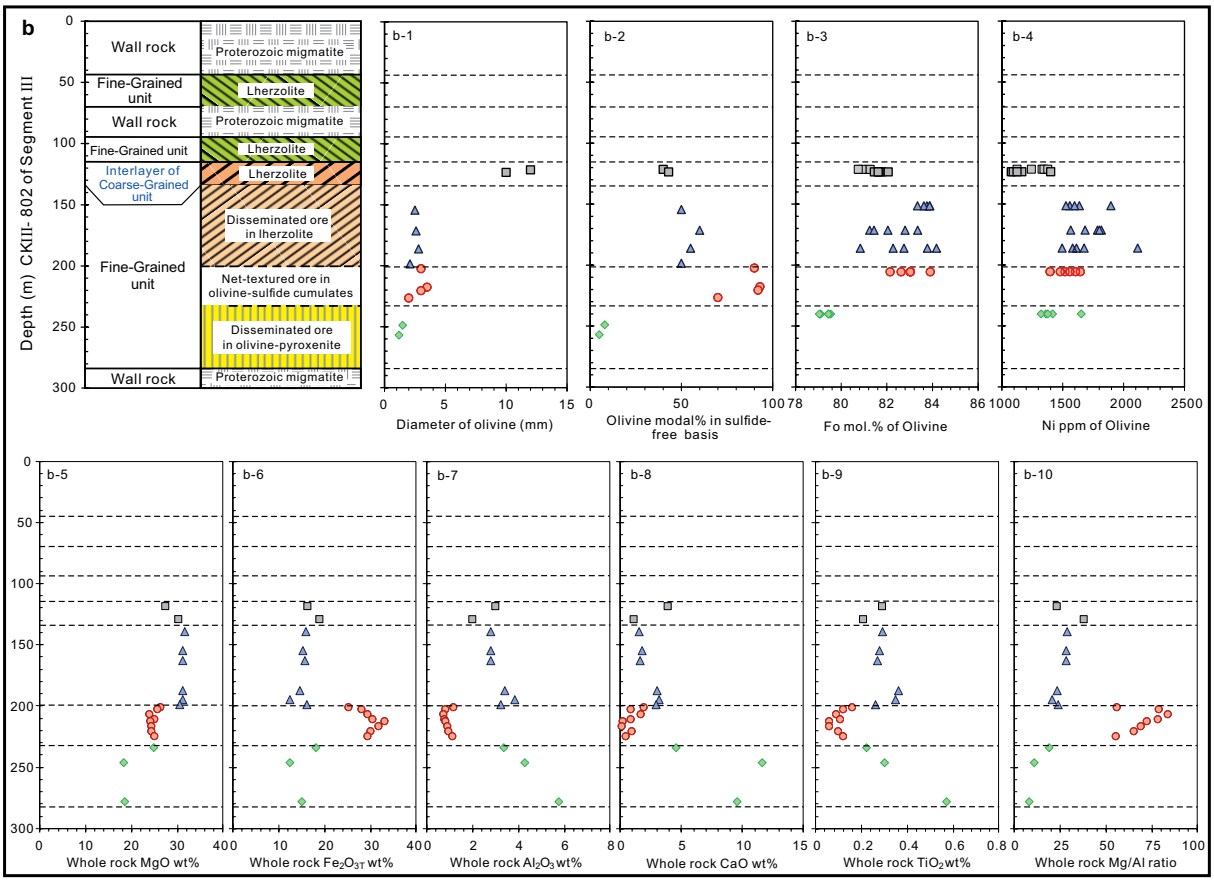

olivine-sulfide cumulates are disordered owing to the effect of the high proportion of sulfides (Fig. 3a-5, a-6, b-5, b-6). The abrupt variations in Mg/Al ratio at the boundary between the olivine-sulfide cumulates and lherzolite reflect a rapid variation in proportions of olivine and pyroxene (Fig. 3a-10, b-10). The coarse-grained lherzolite in the borehole CKIII-503 shows slightly larger ranges of MgO (24.7–30.3 wt %), Al_2O_3 (1.28–2.99 wt %), and TiO_2 (0.13–0.29 wt %) than the fine-grained lherzolite.

Due to potentially large uncertainty in correcting the silicate Fe content for sulfide, only samples contain <5 wt % sulfur are selected in binary plots of MgO against the other oxides (Fig. 5). The whole-rock compositions of these samples have been recalculated to 100% on a volatile-free and sulfide-free basis, and FeO was corrected for Fe associated with sulfide, assuming a molar (Fe + Ni + Cu)/S ratio of 1:1. Iron content in the nonsulfide fraction is expressed as Fe_2O_{3T} except where specified. Due to potentially large uncertainty in correcting the silicate Fe content for sulfide content, olivine-sulfide cumulates containing more than 15% sulfides are excluded in the plotting of Figure 5. These diagrams demonstrate that compositions of the fine-grained sulfide-barren dunite are comparable with those of olivine measured using electron microprobe (Fig. 5), confirming that olivine is the only accumulated silicate mineral in the dunite and that the rocks are meso- to adcumulates such that the olivine composition has not been detectably modified by trapped liquid reaction (Barnes, 1986). Furthermore, the fine-grained and coarse-grained lherzolites plot on linear olivine control lines, indicating that olivine is the predominant cumulus silicate phase in these rocks and that the pyroxenes are primarily derived from trapped intercumulus liquid (Fig. 5). This is consistent with the petrographic observation in lherzolite where olivine is the dominant cumulus phase and clinopyroxene is interstitial to olivine grains (App. Fig. A1a, d). The lherzolites consist of clinopyroxene and olivine in variable compositions with minor orthopyroxene and plagioclase and can be interpreted as olivine orthocumulates.

Chalcophile element geochemistry

The concentrations of Ni, Cu, PGEs, As, Te, and Bi in the sulfide ores are listed in Appendix Table A3. The sulfur contents and Ni and Cu grades of the disseminated ores hosted in the fine-grained lherzolites are obviously lower than those of the net-textured ores hosted in the fine-grained olivine-sulfide cumulates (Fig. 4). It is evident that the net-textured ores in the borehole CKIII-503 have larger variations in Ni, Cu, and PGE grades than those in CKIII-802 due to larger variation in sulfide contents (Fig. 4). The net-textured ores have slightly higher grades of Ir and Ru than the disseminated ores, and they have similar Pt and Pd grades (Fig. 4). However, the disseminated sulfides are enriched over net-textured sulfides in tenors of all PGEs by a factor of around two (App. Figs. A4a, A5). The tenors of PGE of the sulfide ores were recalculated following the methods proposed by Naldrett and Duke (1980) and Song et al. (2009), on the assumption that all of the PGEs were originally present within the sulfide liquid. The error caused by minor amounts of cubanite and pyrite in these samples is negligible. Palladium/Ru values of the disseminated ores in the fine-grained lherzolite vary a little in the two boreholes and tend to decrease upward in the net-textured fine-grained olivine-sulfide cumulates in CKIII-503 (Fig. 4a-9, b-9). The disseminated ores in the coarse-grained lherzolite have large variations in Pt and Pd and relatively constant Ir and Ru.

The disseminated and net-textured ores in the fine-grained lherzolite and olivine-sulfide cumulates have Cu/Pd ratios of 7,500 to 157,000, whereas Cu/Pd ratios of the disseminated ores in the coarse-grained lherzolite range from 20,000 to 160,000 (App. Table A3; Fig. 4a-10, b-10). All of the sulfide ores in the segment III have Cu/Pd ratios much higher than that of the mantle (interquartile range 3,000–8,000; Barnes et al., 2015), indicating parental magmas depleted in PGEs (Barnes and Maier, 1999). The positive correlations between S and the metals indicate that Ni, Cu, and PGE abundances are predominantly controlled by the proportion of cumulus sulfide melt (Fig. 6). The disseminated and net-textured sulfide ores hosted in the fine-grained lherzolite and olivine-sulfide cumulates in segment III are slightly higher in PGE grades and tenors than other three orebodies or similar, respectively (Figs. 6, 7a, b), whereas the sulfide ores in the coarse-grained lherzolite have PGE compositions similar to those of the ores in orebody No. 24 (Figs. 6, 7c) (Chen et al., 2013).

Discussion

Early emplacement of the Fine-Grained unit

It was proposed that Fine-Grained unit formed earlier than the underlying Coarse-Grained unit in the Western intrusion based on the observation of lens-shaped xenolith bodies of the fine-grained dunite incorporated within the lherzolite at the top of Coarse-Grained unit in the open pit of segment I (Song et al., 2012; Chen et al., 2013). Thus, the coarse-grained lherzolite interlayers within the fine-grained olivine-sulfide cumulates or lherzolite in segment III were most likely the result of intrusion of the Coarse-Grained unit into the Fine-Grained unit (Fig. 2d). This is supported by the sharp contacts between the coarse-grained lherzolite and fine-grained olivine-sulfide cumulates and lherzolite indicated by the significant differences in modal % and forsterite values of the olivine and differences in whole-rock compositions (Fig. 3). The different whole-rock compositions between the coarse-grained lherzolite and the fine-grained olivine-sulfide cumulates reflect their different trapped liquid abundances (Fig. 3a), the net-textured ore being olivine-sulfide adcumulates and the lherzolites being olivine orthocumulates. The relatively low forsterite values of the olivine in the coarse-grained lherzolite demonstrate that olivine in the orthocumulates experienced more extensive reequilibration with interstitial silicate liquids than in the olivine-sulfide cumulates (Barnes, 1986).

Fig. 4. Stratigraphic columns of whole-rock contents of S, Ni, Cu, Ni/Cu, PGEs, Pd/Ru, and Cu/(Pd × 1,000) of the drill holes (a) CKIII-503 and (b) CKIII-802. The purple dotted lines represent variation of Ni and Cu grades (data from exploration report of segment III of Jinchuan Group Ltd., 2020).

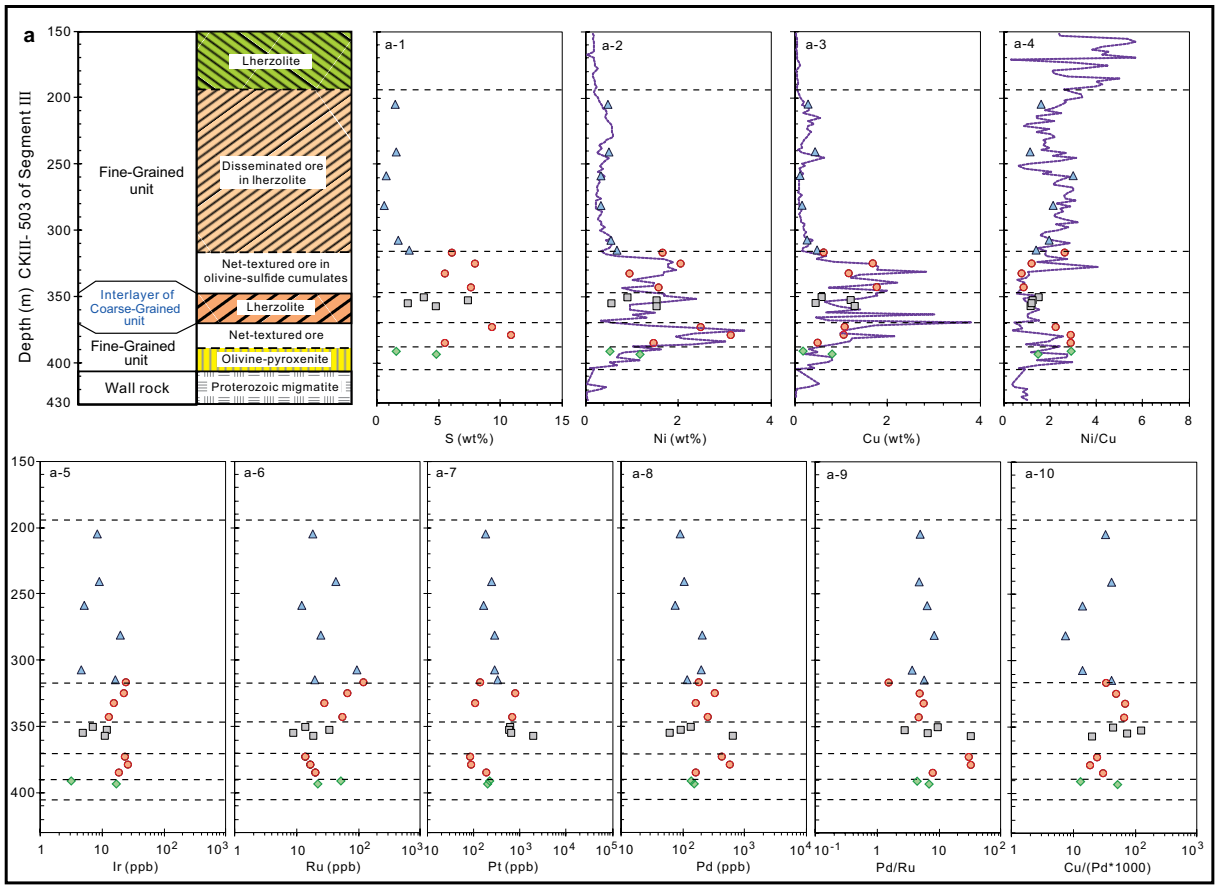

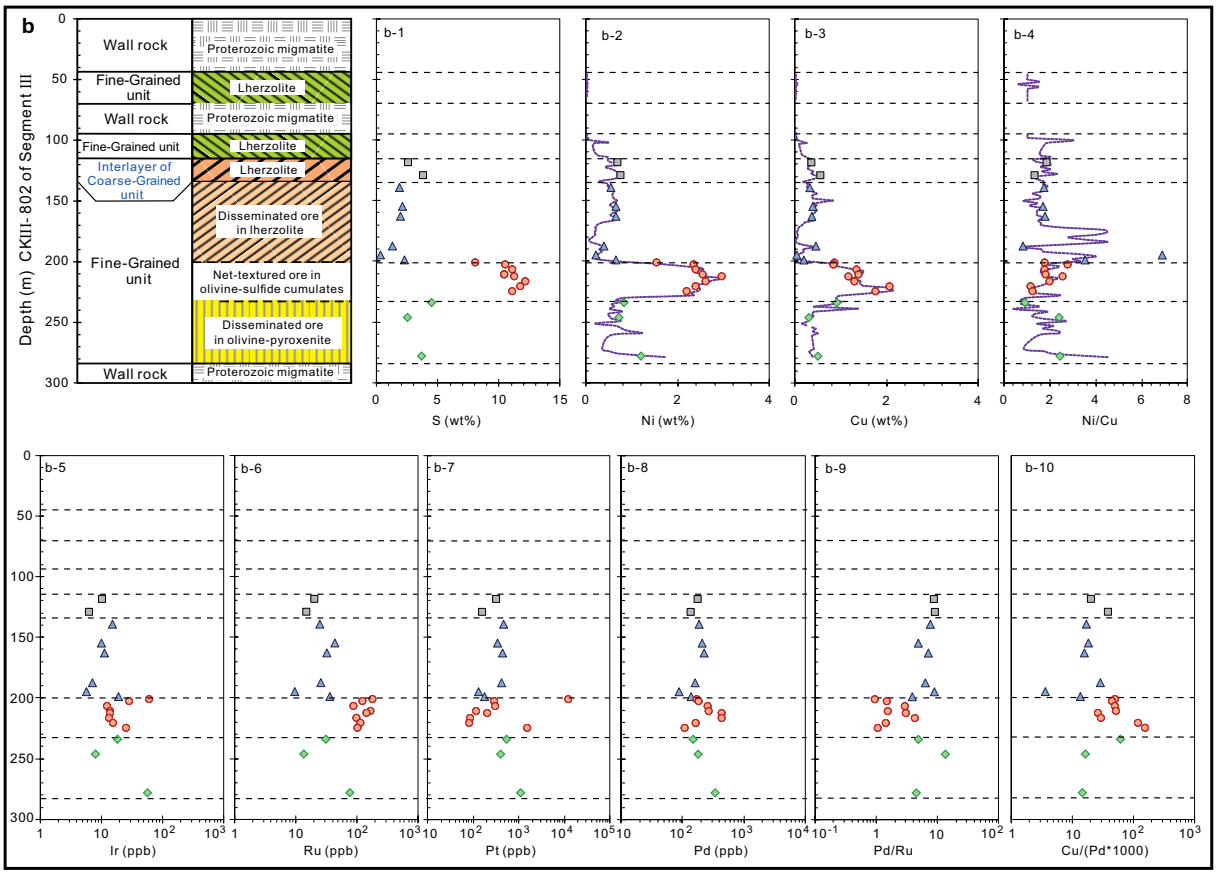

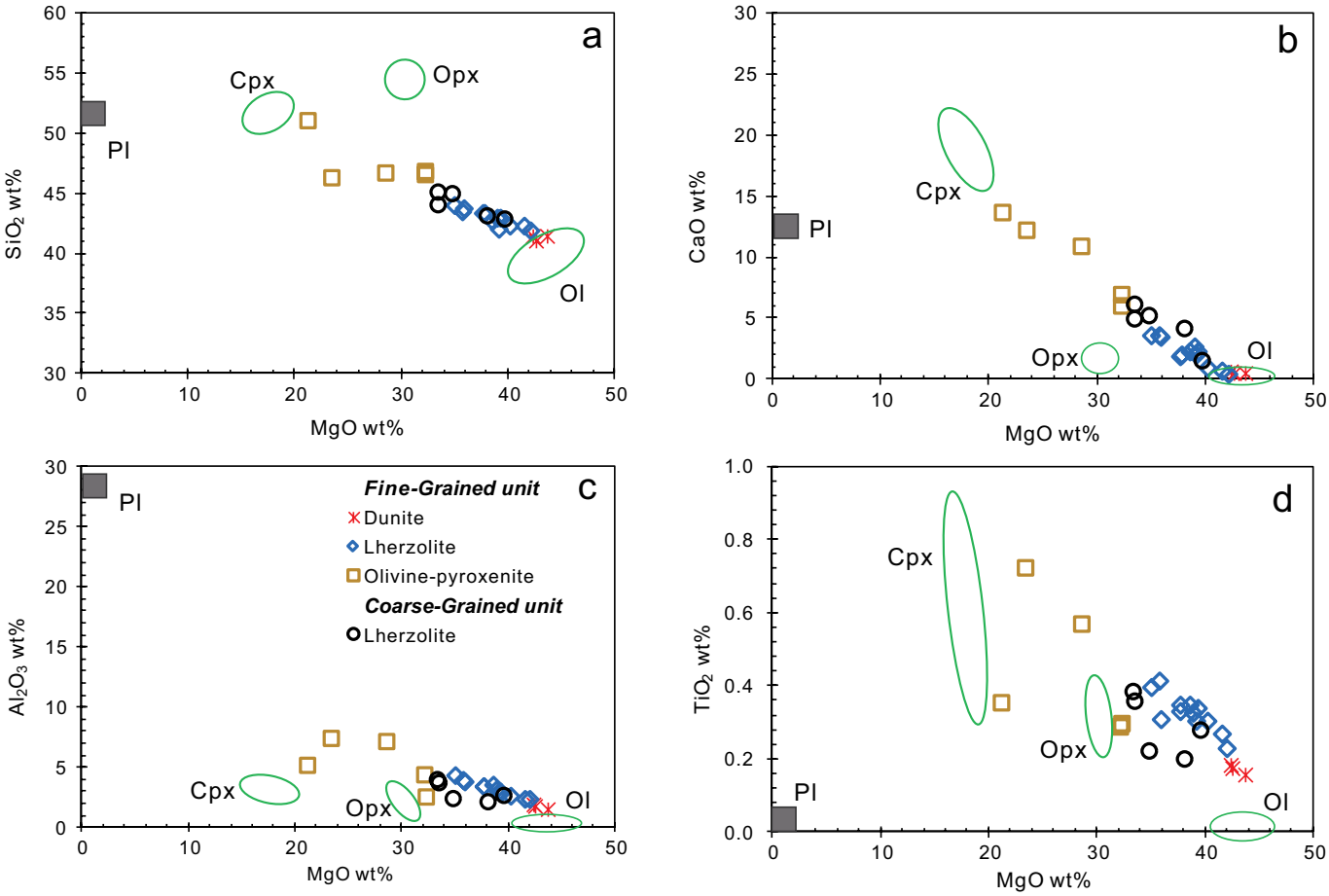

Fig. 5. (a-d) Binary plots of MgO versus SiO_2 (a), CaO (b), Al_2O_3 (c), and TiO_2 (d) for the samples with <5% sulfur from segment III. The oxide contents are normalized to 100% on anhydrous and sulfide-free basis. Samples with >5% S excluded. The data of mineral compositions are after Li (2008), Chen (2009), and Tonnelier (2010). Abbreviations: Cpx = clinopyroxene, Ol = olivine, Opx = orthopyroxene, Pl = plagioclase.

Hydrothermal alteration and nugget effects on PGEs

The appearances of hydrophases, such as serpentine, chlorite, tremolite, etc., indicate that the olivine-sulfide cumulates and lherzolite in segment III have experienced extensive hydrothermal alteration (App. Fig. A1). Negative $\delta^{34}S$ values of the pyrite in the Jinchuan deposit indicated that the pyrite was formed by hydrothermal alteration (Ripley et al., 2005; Li and Ripley, 2011). During the alteration, magnetite and pyrite were formed via reaction between the base-metal sulfides and hydrothermal fluids (App. Fig. A2) (Djon and Barnes, 2012):

$$6FeS\ (\text{pyrrhotite}) + 2O_2 = Fe_3O_4\ (\text{magnetite}) + 3FeS_2\ (\text{pyrite}). \quad (1)$$

It is generally agreed that the iridium-group PGEs were immobile in hydrothermal alteration, whereas Cu, Au, Pt, and Pd could be transported in hydrothermal fluids (Keays et al., 1982; González-Álvarez et al., 2013; Keays and Jowitt, 2013; Pirajno and González-Álvarez, 2013). Although several factors (including oxygen fugacity, pH, and salinity; Barnes and Liu, 2012) may affect the solubility of Pt and Pd in hydrothermal fluid, Pd is more soluble than Pt under common conditions (Godel et al., 2007; Barnes and Liu, 2012; Keays and Jowitt, 2013; Le Vaillant et al., 2015, 2016; Holwell et al., 2017).

However, remarkable negative and positive Pt anomalies and decoupling between Pt and Pd in the net-textured ores (Fig. 7b; App. Fig. A4) indicate that Pt is likely more variable in orebody No. 3 within segment III. The roughly positive correlations of Pt with As and Bi + Te for most of the sulfide ores from the segment III (App. Fig. A6a, c) indicate that Pt is mostly contained by minerals of arsenide, sulfarsenide, telluride, and bismuthide (Sixth Geological Unit, 1984; Chai et al., 1993; Prichard et al., 2013; Chen et al., 2015; Yang et al., 2017). However, three net-textured ores are extremely high in Pt and low in As and Te + Bi, indicating dissolution of the Pt minerals and suggesting that migration of Pt or Pt occurs as sulfides or Pt-Fe alloy in these samples (App. Fig. A6a, c). In contrast, the sulfide ores show good positive correlations of Pd with As or Te + Bi (App. Fig. A6b, d). In alteration, the large variation of the net-textured ores in Pt can also be explained by nugget effects due to heterogeneous distribution of Pt minerals (Barnes et al., 2022), arising from the very strong tendency of Pt to form its own minerals, such as Pt-Fe alloy. Duplicate analyses of a few samples give consistent PGE contents in this study (App.

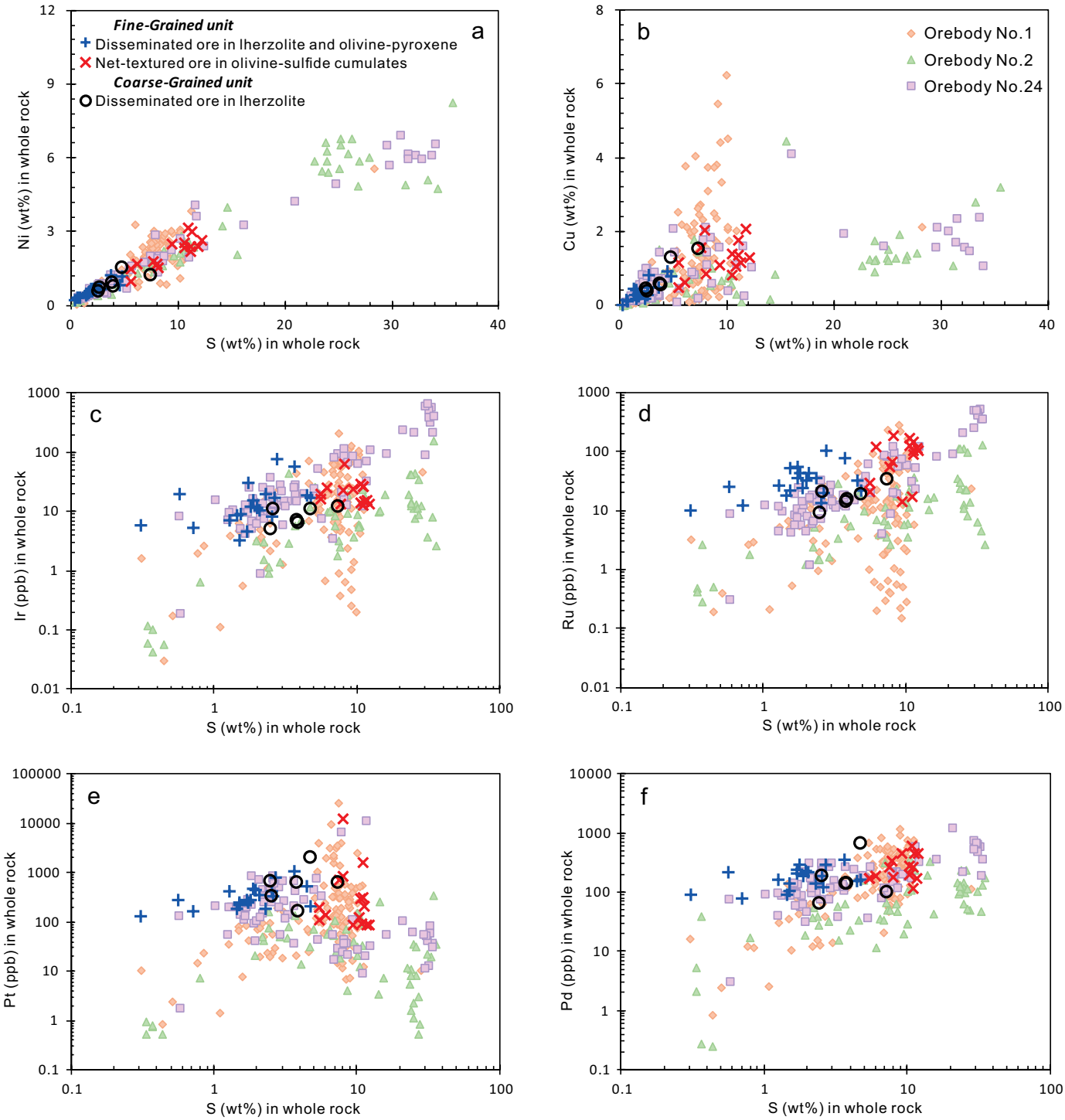

Fig. 6. Binary plots of S versus Ni (a), Cu (b), Ir (c), Ru (d), Pt (e), and Pd (f) for the sulfide ores from orebody No. 3 in segment III. Data of the orebodies No. 1, 2, and 24 are from Chai and Naldrett (1992b), Song et al. (2009), Tonnelier (2010), Chen et al. (2013), and Duan et al. (2016).

Table A3), but the nugget effect could not be ruled out completely. The Pt minerals in segment III probably were large and homogenized when the net-textured ores were milled to –200 mesh powders. Thus, the nugget effect is not evident from duplicate measurements on pulps from the same coarse sample split.

A similar observation of larger variation in Pt than in Pd was also made on the net-textured and massive ores from the orebodies No. 1, No. 2, and No. 24 at Jinchuan (Song et al., 2009; Chen et al., 2013). Minerals of Pt and semimetals were discovered enclosed in base metal sulfides or at the boundaries of the sulfides at Jinchuan (Prichard et al., 2013; Chen et al.,

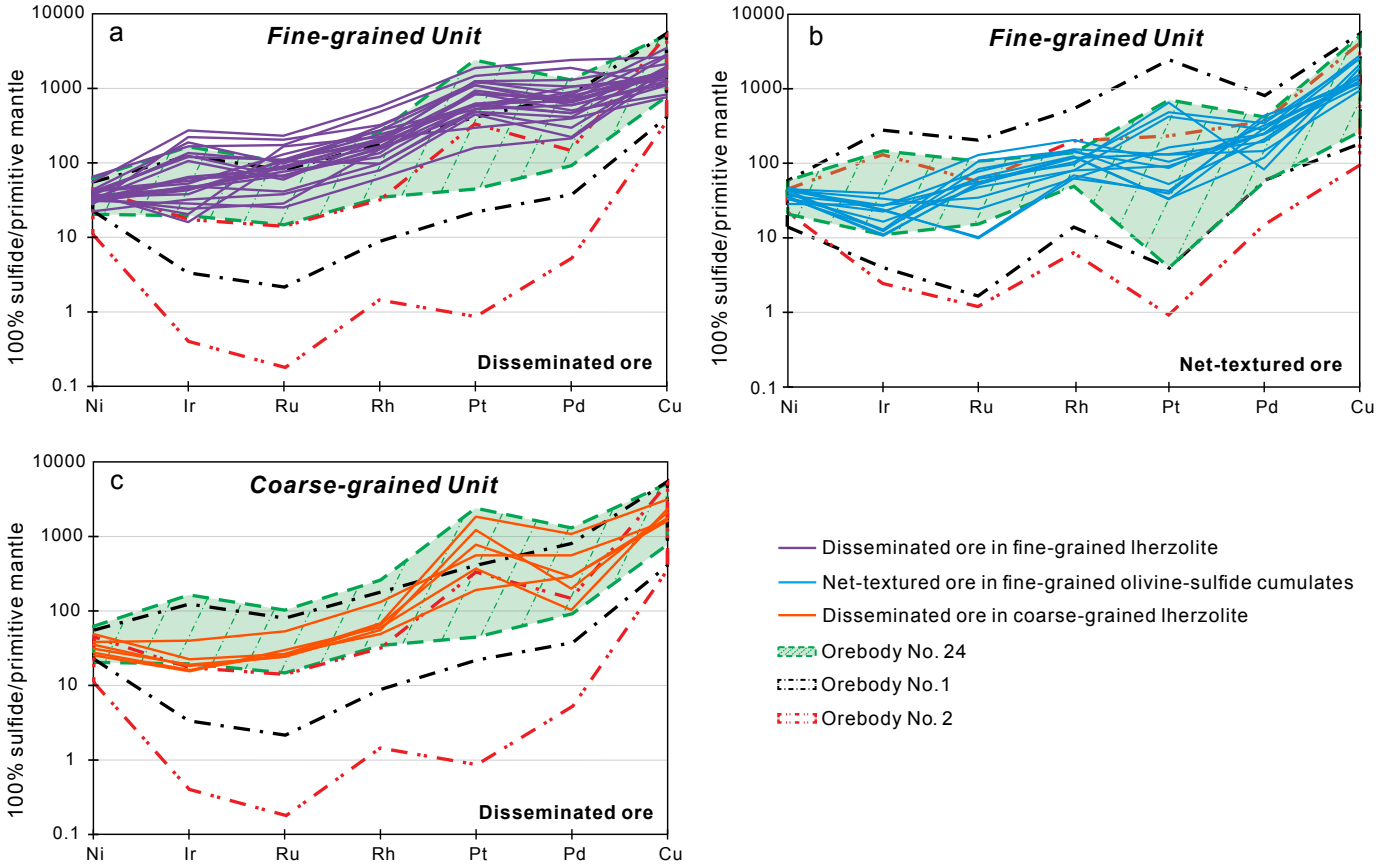

Fig. 7. (a-c) Primitive mantle-normalized Ni, platinum group element, and Cu patterns of the disseminated and the net-textured ores from orebody No. 3 on a 100% sulfide. Primitive mantle values of the metals are from Barnes and Maier (1999). The data of the orebodies No. 1, 2, and 24 are from Chai and Naldrett (1992b), Song et al. (2009), Tonnelier (2010), Chen et al. (2013), and Duan et al. (2016).

2015). The decoupling between Pt and Pd was interpreted as removal of Pt-Fe alloys together with chromite prior to sulfide saturation and postmagmatic hydrothermal alteration (Su et al., 2008; Song et al., 2009; Yang et al., 2017), although nugget effects could also have played a role here.

Olivine compositions and implications

Continuous supply of magma was recognized in the Coarse-Grained unit of the Western intrusion (Chen et al., 2013). The slightly higher forsterite values of the olivine in the fine-grained lherzolite than in the underlying olivine-sulfide cumulates in the boreholes CKIII-503 and CKIII-802 indicate that magma supplement also occurred in the Fine-Grained unit (Fig. 3). However, the small differences of forsterite values of the olivine in both the olivine-sulfide cumulates and lherzolite imply that they are cumulates derived from magmas with similar compositions. The abrupt decreases of olivine contents, appearance of clinopyroxene (App. Fig. A1), and increase of whole-rock Al_2O_3 and CaO contents from the fine-grained olivine-sulfide cumulates to lherzolite are related to a higher proportion of trapped intercumulus liquid, which is manifested by sharp decrease of Mg/Al values (Fig. 3a-10, b-10). In the diagram of the atomic ratios of (Mg + Fe)/Ti against Si/Ti (Pearce, 1968), most of the segment III rocks plotted close to a line with a slope of 2, indicating that olivine is the primary cumulate phase (Fig. 8a). Three fine-grained olivine-pyroxenites fall off this line, indicating that these are probably accumulation of olivine and clinopyroxene and/or plagioclase or that they are formed by alteration. Positive correlations of the atomic ratios of Mg/Ti and Fe/Ti indicate that the lherzolites and dunites can be interpreted as cumulates of olivine with near-constant composition, providing further evidence that they formed from the same magma. Regression of Mg/Ti on Fe/Ti indicates this cumulus olivine had a forsterite content of 86.7 ± 0.75 (2σ) mol % (Fig. 8b). Based on the plot of MgO and FeO (Chai and Naldrett, 1992a) and assuming an olivine-liquid Fe/Mg K_D (= $(FeO/MgO/MgO)^L$) of 0.3 (Roeder and Emslie, 1970), the best estimate for the parental magma in equilibrium with this olivine contained ~8 to 10% MgO and 8 to 9% FeO (Fig. 8c). The interstitial pyroxenes in the lherzolites were the result of crystallization of the trapped magma, as concluded by Mao et al. (2018a). Therefore, the modal % of the pyroxenes in the lherzolite (App. Fig. A1c, d) reflect the variable proportions of the trapped silicate liquid between olivine crystals.

Chalcophile element compositions of the parental magmas

The disseminated sulfides can provide extra constraints on the nature of the parental magma because their compositions are not modified by extensive fractionation of sulfide liquid

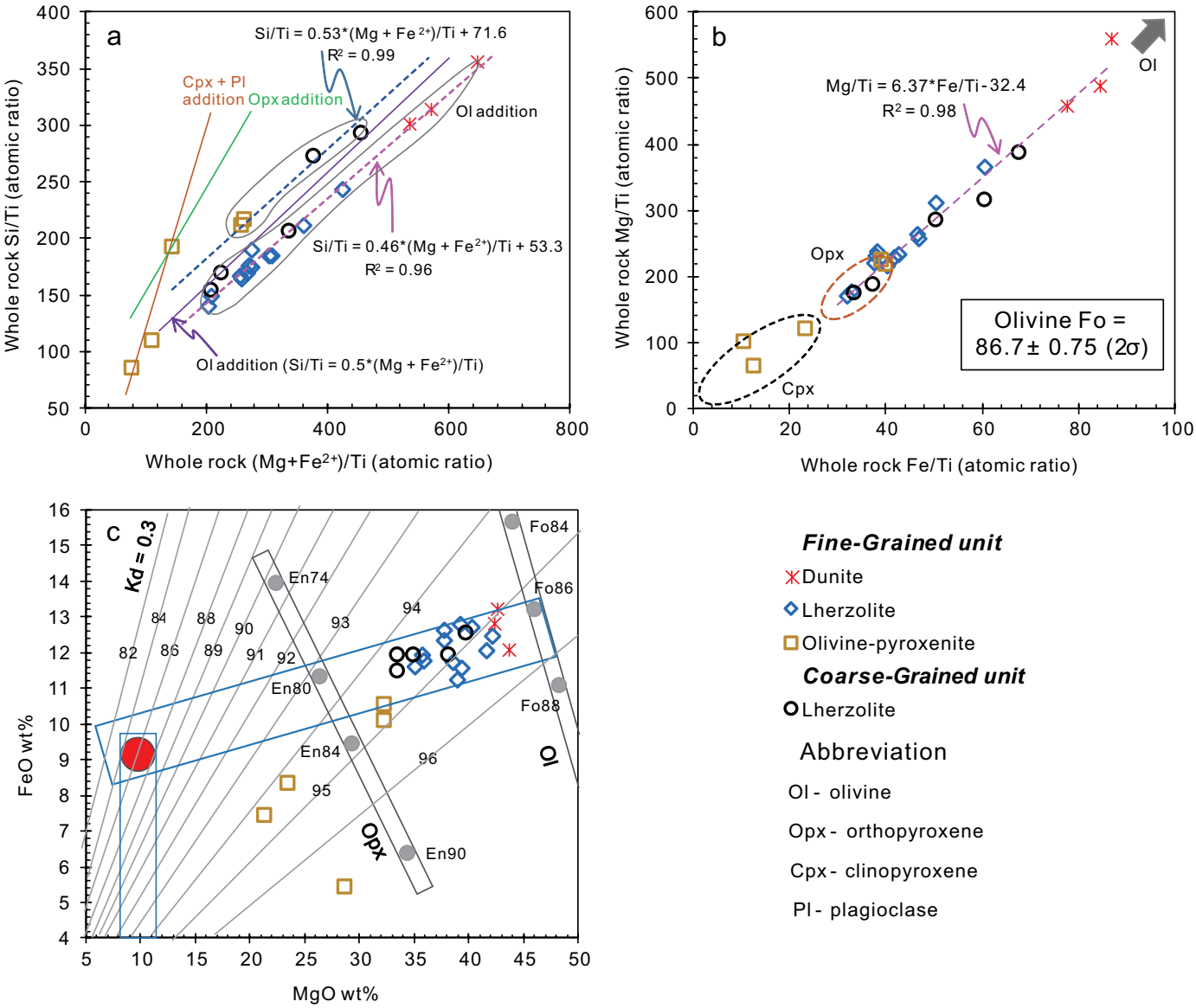

Fig. 8. (a) Correlation of Si/Ti versus (Mg + Fe^{2+})/Ti (whole-rock atomic ratios) for the samples from segment III, showing that dunite and lherzolite fall almost exactly on olivine control lines (blue and magenta color). All Fe in the rocks is assumed to be present as FeO on the grounds that the rocks are cumulates. The fine-grained olivine-pyroxenites fall off the olivine control lines, indicating that they are probably accumulation of olivine, clinopyroxene, and plagioclase (orange line). (b) Correlation of Mg/Ti versus Fe/Ti (whole-rock atomic ratios) defines a slope, which gives Fe/Mg ratio of average cumulus olivine with forsterite (Fo) = 86.7 ± 0.75 (2σ) in olivine trend samples. The black and orange dashed circles represent compositions of the clinopyroxene and orthopyroxene at Jinchuan, respectively (Li, 2008; Chen, 2009; Tonnelier, 2010). (c) Plots of FeO versus MgO of whole-rock in sulfide-free basis for the samples from segment III. Olivine control samples generate a trend between olivine with Fo = 86 to 87 and liquid with ~9 to 11% MgO, 8 to 9% FeO. Sloping gray lines indicating MgO-FeO ratios of liquid compositions in equilibrium with the indicated olivine forsterite content (Kd = $(FeO/MgO)^{olivine}/(FeO/MgO)^{magma}$ = 0.3 ± 0.03). The lines labeled Opx and Ol represent pure orthopyroxene and olivine compositions respectively. Kd represents the Fe-Mg distribution coefficient between olivine and liquid. En represents the percentage of enstatite in orthopyroxene.

(Barnes and Maier, 1999), such that they are a reliable estimate of the original composition of the sulfide liquid. The Cu/Pd ratios of the disseminated sulfides of orebody No. 3 in the Fine-Grained unit ranged from ~14,000 to ~40,000 (25th and 75th percentiles), which is lower than the Cu/Pd ratios of the disseminated sulfides of the orebody No. 24 in the Coarse-Grained unit (~30,000–60,000, 25th and 75th percentiles) (App. Fig. A4b) (Chen et al., 2013). These values are much higher than Cu/Pd of mantle samples (3,000–8,000) (Barnes et al., 2015), indicating that the sulfide liquid component was depleted by about an order of magnitude in Pd over Cu due to prior extraction of sulfide. Based on compositions of the olivine and the sulfide tenors, it is estimated that the parental magma of the Fine-Grained unit contained ~200 ppm Ni, ~150 ppm Cu, and ~3.5 ppb Pd, which was produced by removal of ~0.001% sulfide from a high-Mg basaltic magma

containing ~10 ppb Pd, ~1 ppb Ru, and ~200 ppm Ni (Chen et al., 2013; Yao et al., 2018). The lower Cu/Pd ratios of the disseminated ores in the fine-grained lherzolite imply that the parental magma of the Fine-Grained unit was slightly less depleted in PGEs than that of the Coarse-Grained unit due to less preemplacement sulfide removal.

Sulfide tenors and fractional crystallization of sulfide melt

Variability in ore tenors can be the result of primary liquidus variability controlled by magma composition and R factor, but wide variability can also be generated within orebodies by sulfide liquid fractionation (Naldrett, 2004; Barnes et al., 2017b), which causes dispersion in ratios between Ni and Cu and between the PGEs. Experimental studies have confirmed that Os, Ir, Ru, and Rh tend to partition into monosulfide solid solution (MSS) during fractional crystallization of sulfide liquid, whereas Pt, Pd, Au, and Cu behave incompatibly and tend to concentrate in the residual sulfide liquid (Barnes et al., 1997; Mungall et al., 2005; Godel and Barnes, 2008; Helmy et al., 2010; Mansur et al., 2020). Therefore, variations of Pd/Ru values of the sulfide ores reflect the degree of fractional crystallization of MSS. The negative correlations of Ru versus Pd/Ru and positive correlation of Pd versus Pd/Ru for the net-textured fine-grained olivine-sulfide cumulates of orebody No. 3 (Fig. 9a, b) indicate dispersion of inter-PGE ratios due to fractional crystallization of MSS. This is evidenced by the positive correlation between Pd/Ru and Ni/Ru ratios for the net-textured ores in the fine-grained olivine-sulfide cumulates (Fig. 9c). However, the apparent enrichment of Ru and Pd of the disseminated ores in the fine-grained lherzolite combined with small ranges of Pd/Ru ratios (Fig. 9a, b) indicate that the sulfide liquid component of these ores was enriched in PGEs overall prior to sulfide liquid differentiation. This could reflect two possible processes: formation at higher effective R values (Fig. 10) due to more vigorous mixing in a higher-energy flow or upgrading of PGEs by reaction with successive pulses of fresh magma; these two processes cannot be distinguished on the basis of sulfide composition (Mungall et al., 2020). If the upgrading mechanism is preferred, this implies that the sulfides in the net-textured ores were separated from further reaction with the basaltic magmas after deposition, whereas the sulfides in the disseminated ores continued to react with undepleted magma. The model curves in Figure 10 indicate that the effect of including olivine in the silicate-sulfide mass balance calculation, combined with a difference in R factor, can account for the difference between Ni and Pd tenors in net-textured and disseminated sulfide, within the constraint provided of the silicate and olivine geochemistry that they formed from essentially the same magma.

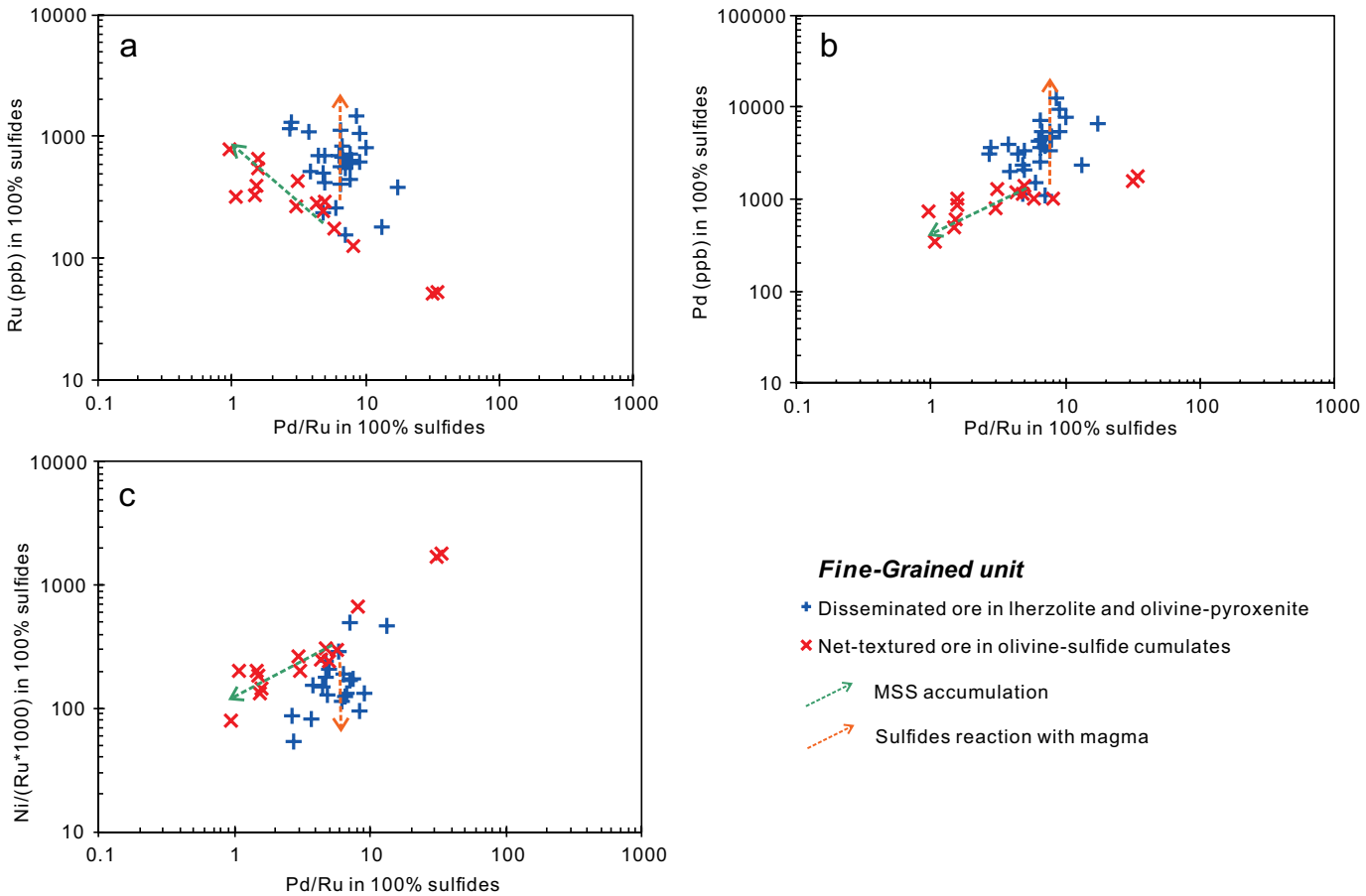

Fig. 9. Correlations of Pd/Ru versus Ru (a), Pd/Ru versus Pd (b), and Ni/(Ru × 1,000) versus Pd/Ru (c) for the sulfide ores from orebody No. 3 in 100% sulfide basis. MSS = monosulfide solid solution.

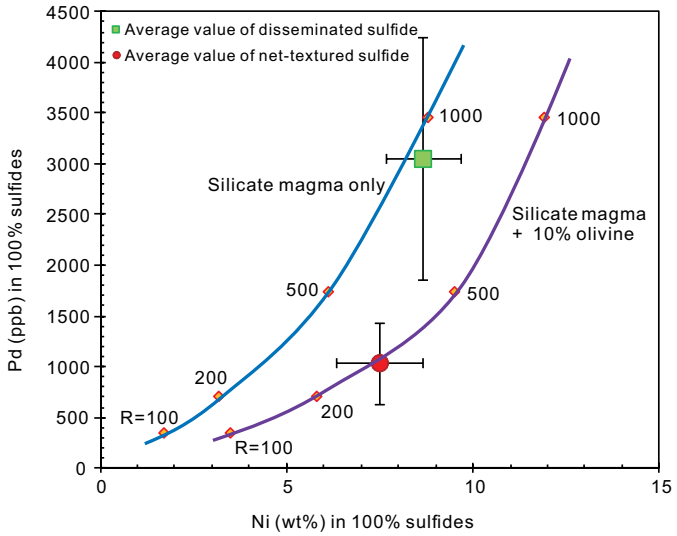

Fig. 10. Modeling for R factor combined with Fe-Ni exchange during batch equilibration between sulfide liquid, silicate liquid, and olivine. The simulation assumes a silicate melt with 10% MgO, 9% FeO, 200 ppm Ni, 150 ppm Cu, 3.5 ppb Pd, and fo_2 at quartz-fayalite-magnetite buffer (QFM) +1 by the method of Barnes et al. (2013) and Mao et al. (2018b). R value is the mass ratio of silicate melt to sulfide melt involved in the reaction. Model curves are for equilibrium between sulfide liquid and silicate liquid only (blue curve) or between sulfide liquid and a mixture of 90% silicate liquid and 10% olivine (purple curve). The compositions of olivine and sulfide are calculated according to the program proposed by Barnes et al. (2013). Average ore tenors are shown with the green box and the red circle with error bars of 2σ uncertainty.

Sulfide deposition in the fine-grained olivine-sulfide cumulates and lherzolite

As described above, in orebody No. 3, the net-textured sulfide ores are hosted by fine-grained olivine-sulfide cumulates that simply consists of sulfides and olivine with minor pyroxene, whereas the disseminated sulfides are hosted in fine-grained lherzolite or olivine-pyroxenite. In other words, the net-textured sulfide ore is an olivine-sulfide liquid adcumulate, whereas the fine-grained lherzolite/olivine-pyroxenite is an olivine/clinopyroxene-sulfide liquid orthocumulate. However, both the lherzolite and olivine-sulfide cumulates have similar parental magmas, as attested by similar forsterite values of the olivine (Fig. 3), indicating that the difference between them is solely due to the higher trapped liquid proportion in the lherzolite.

Modeling calculations indicate that fractional crystallization alone could not trigger sulfide saturation in the Jinchuan parental magma without addition of external sulfur (Duan et al., 2016). However, the country rocks at Jinchuan are poor in sulfur (<100 ppm S) (Ripley et al., 2005). Thus, sulfide immiscibility in the Jinchuan system is generally regarded as having occurred at deep levels, and the sulfide liquids were carried upward by the basaltic magmas (Tang, 1991; Ripley et al., 2005; Song et al., 2009). When the magma carrying sulfide droplets intruded into the Western intrusion, reaction with the wall rock, migmatite, resulted in compositional changes of the magma. More pyroxene could be crystallized from such magma to form olivine-pyroxenite at the bottom of magma chamber. Thus, the olivine-pyroxenites in segment II have $\delta^{18}O$ values from 6.5 to 7.8‰ (Ding et al., 2021), which is different from that of the mantle ($\delta^{18}O$ = 5.3 ± 0.6‰) (Eiler, 2001; Valley et al., 2005).

A perplexing question is what mechanisms resulted in the different styles of mineralization in the olivine-sulfide cumulates and lherzolite in orebody No. 3. The net-textured olivine-sulfide cumulates and lherzolite containing disseminated sulfides also occur in the orebodies No. 1 and No. 24 in segments II and I, respectively (Song et al., 2009; Chen et al., 2013). A recent study by Mao et al. (2018a) indicated that olivine is the primary cumulate phase in both the olivine-sulfide cumulates and lherzolite in segments I and II. Crystal size distributions of olivine in the lherzolite containing disseminated sulfides are indistinguishable from those in the olivine-sulfide cumulates containing net-textured sulfides from both segments. They attributed the formation of the net-textured olivine-sulfide cumulates to percolation of sulfide liquid through the pore space of the olivine framework, expelling the interstitial silicate liquid, after significant (40–70%) olivine crystallization.

In orebody No. 3, the fine-grained net-textured olivine-sulfide cumulates are overlain by the fine-grained lherzolite containing disseminated sulfides, and olivine is the primary cumulate phase in both (Fig. 8). This is similar to the lherzolite and olivine-sulfide cumulates in segments I and II (Mao et al., 2018a). Thus, we envisage that a similar process could have occurred not only in segments I and II but also in segment III. Cumulus olivine and sulfide liquid was deposited at the bottom of the magma chamber (Fig. 11a). Then, gravity-driven percolation of sulfide liquid took place through the pore space of the olivine cumulate, expelling the silicate melt upward (Fig. 11b; App. Fig. A1e). This process is self-reinforcing because of the interplay of gravitational force on the droplets, the opposing capillary force resisting percolation through small pores, and progressive coalescence of droplets into elongate connected tubes with progressively greater hydrostatic head driving the percolation (Fig. 11b) (Mungall and Su, 2005; Barnes et al., 2017a). In this interpretation, the olivine-sulfide cumulates were formed by very extensive displacement of the interstitial silicate melt in the olivine cumulates by the percolating sulfide liquid. The overlying lherzolite was formed by crystallization of the interstitial melt among the olivine cumulates and reaction with olivine grains. Thus, the olivine in the lherzolite is always poikilitic within large anhedral pyroxene (Fig. 11c; App. Fig. A1a-d). The disseminated sulfides in the lherzolite remained in diffusive contact with flowing magma above and hence became upgraded in PGEs (Fig. 9; App. Fig. A5).

The drawback of this simple model of single-stage accumulation followed by percolation and silicate melt displacement is that the disseminated sulfides in the lherzolite and the net-textured olivine-sulfide cumulates have different compositions. The disseminated sulfides are more enriched in Pd than the net textured sulfides, have moderate Pd/Ru, and are slightly enriched in Ni (Figs. 9, 10). A systematic difference could be explained within a simple percolation model if the sulfide liquid were fractionating during the percolation process, but this would tend to generate sulfides with higher Pd and higher Pd/Ru in the more extensively percolated sulfide deeper in the cumulate pile, i.e., in the net-textured ores. This is the opposite of what is observed in the drill hole CKIII-802,

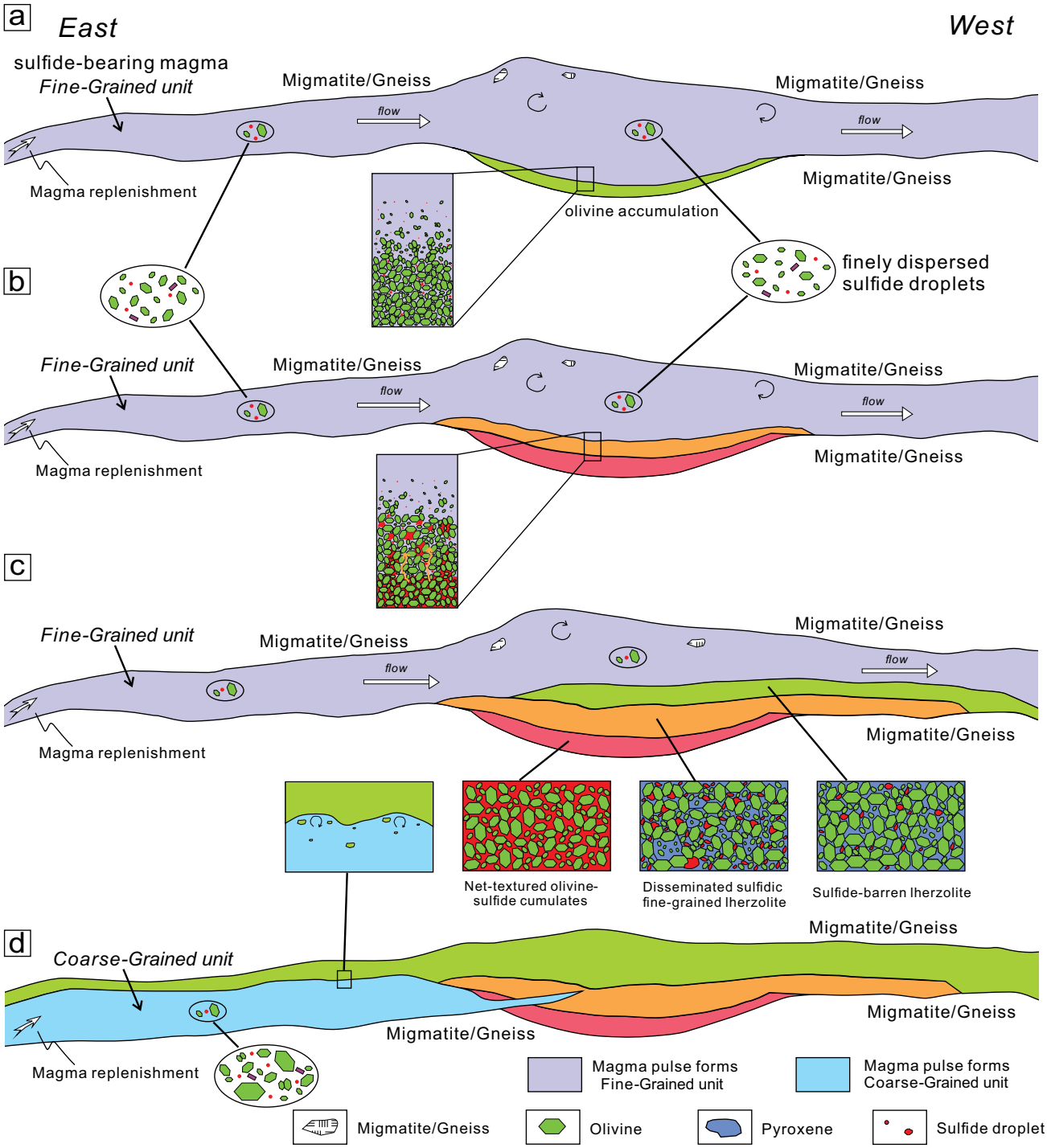

Fig. 11. Model for the formation of orebody No. 3. (a) Olivine accumulated at the bottom of the flowing magma as the predominant cumulate phase. (b) Coalescing sulfide droplets percolated through the olivine crystal mush and expelled the silicate melt upward. Downward percolation of sulfide and upward percolation of silicate magma could product an ore profile of net-textured to disseminated ores gradually upward. (c) The overlying lherzolite was formed by crystallization of interstitial silicate melt among the olivine cumulates. The disseminated ores could have been upgraded by entrainment and redeposition. (d) The later magma forming the Coarse-Grained unit intruded along the lower boundary of the Fine-Grained unit. The interlayer of the Coarse-Grained unit is formed by magma flowing into the Fine-Grained unit.

in which Pd/Ru values of the net-textured olivine-sulfide cumulates are lower than those of the disseminated sulfidic lherzolite and show irregular variation (Fig. 4b-9). The implication is that the sulfides that were accumulating along with the olivine changed in composition (Fig. 9), becoming enriched in both PGEs and Ni. The model calculation in Figure 10 shows that an increase in R factor from around 300 to around 800 could explain the difference (also allowing for a

variable contribution of Ni from olivine to the mass balance), with the disseminated ores having reacted with the greater volume, potentially during ongoing reaction between the flowing magma and the crystal-sulfide slurry at the top of the crystal pile.

The two models—variable degree of silicate-sulfide reaction and percolation to form net-textured ores—are not mutually exclusive. It is likely that accumulation and percolation would be occurring on similar timescales, such that earlier formed sulfides had already percolated to form net-textured ores while disseminated ores were still accumulating above them.

A third possibility is that the net-textured ores were formed by accumulation of wetting of olivine by sulfide liquid during entrainment and transport, followed by settling of olivine-sulfide clumps. The olivine grains or clusters wrapped by sulfide liquid would settle through a liquid column more quickly than individual olivine grains or sulfide droplets owing to their larger effective grain size and density of olivine-sulfide clusters. However, experiments on wetting of olivine by silicate melt and sulfide liquid (Mungall and Su, 2005), consideration of surface tension effects (Chung and Mungall, 2009), and 3-D morphologies of sulfide droplets in olivine orthocumulates and adcumulates (Barnes et al., 2017a) indicate that silicate melt preferentially wets olivine relative to sulfide liquid, impeding the tendency for sulfide melt to coat olivine grain surfaces when suspended in a silicate magma. Thus, this hypothesis needs to be further tested, although it could explain the abrupt variations between the fine-grained olivine-sulfide cumulates and lherzolite in modes of olivine and contents of sulfide and metals (Figs. 3, 4).

Although the parental magmas of Fine-Grained and Coarse-Grained units in the Western intrusion have similar compositions, two stages of mineralization are indicated. The early sulfide mineralization formed the orebody No. 3 in the bottom of the Fine-Grained unit of the Western intrusion (Fig. 11a-c). The following pulse of magma intruded along the base of the Fine-Grained unit and formed the Coarse-Grained unit, and deposition of sulfides produced the orebody No. 24 at the bottom (Fig. 11d). The Fine-Grained and Coarse-Grained units are dominant in the west and east portions of the Western intrusion and mainly constitute segments III and I, respectively (Figs. 2, 11).

Conclusion

The newly discovered orebody No. 3 occurs in the Fine-Grained unit of the Jinchuan Western intrusion and is independent from the orebody No. 24, which occurs in the Coarse-Grained unit. The Fine-Grained unit was formed by continuous influx of basaltic magma in a dynamic conduit system. Olivine is the primary cumulate phase in the Fine-Grained unit. The net-textured olivine-sulfide cumulate comprises fine-grained olivine enclosed by sulfides and was most likely formed by downward percolation of sulfide liquids into the intercumulus pore space, displacing the interstitial silicate melt. In contrast, the fine-grained lherzolite containing disseminated sulfides was formed by deposition of fine sulfide droplets along with olivine and crystallization of pyroxene from interstitial silicate melts. Higher PGE tenors of the disseminated ores relative to the net-textured ores are attributed to PGE upgrading via reaction between sulfide droplets and magmas or due to larger ratios of silicate/sulfide liquids at the deposition stage. The variations of PGE tenors within the net-textured ores result from differentiation of the sulfide liquid during percolation.

Acknowledgments

This study is supported by National Science Foundation of China projects (41630316 and 41772067 to X.-Y. Song) and the Strategic Priority Research Program (B) of the Chinese Academy of Sciences (XDB18000000). We are grateful to L. Qi, D.-P. Wang, Y. Huang, T.-X. Zhang, K.-Z. Wang, and X.-D. Li for their help in analyses of PGE contents and field work. Constructive reviews from Dr. Louise Schoneveld and an anonymous reviewer and editorial guidance from Dr. Eduardo Mansur (guest editor) are greatly appreciated.

REFERENCES

Barnes, S.-J., and Maier, W.D., 1999, The fractionation of Ni, Cu and the noble metals in silicate and sulfide liquids: Geological Association of Canada Short Course, v. 13, p. 69–106.

Barnes, S.-J., Makovicky, E., Makovicky, M., Rose-Hansen, J., and Karupmoller, S., 1997, Partition coefficients for Ni, Cu, Pd, Pt, Rh, and Ir between monosulfide solid solution and sulfide liquid and the formation of compositionally zoned Ni-Cu sulfide bodies by fractional crystallization of sulfide liquid: Canadian Journal of Earth Science, v. 34, p. 366–374.

Barnes, S.J., 1986, The effect of trapped liquid crystallization on cumulus mineral compositions in layered intrusions: Contributions to Mineralogy and Petrology, v. 93, p. 524–531.

Barnes, S.J., and Liu, W., 2012, Pt and Pd mobility in hydrothermal fluids: Evidence from komatiites and from thermodynamic modelling: Ore Geology Reviews, v. 44, p. 49–58.

Barnes, S.J., Godel, B., Gürer, D., Brenan, J.M., Robertson, J., and Paterson, D., 2013, Sulfide-olivine Fe-Ni exchange and the origin of anomalously Ni rich magmatic sulfides: Economic Geology, v. 108, p. 1971–1982.

Barnes, S.J., Mungall, J.E., and Maier, W.D., 2015, Platinum group elements in mantle melts and mantle samples: Lithos, v. 232, p. 395–417.

Barnes, S.J., Mungall, J.E., Vaillant, M.L., Godel, B., Lesher, C.M., Holwell, D., Lightfoot, P.C., Krivolutskaya, N., and Wei, B., 2017a, Sulfide-silicate textures in magmatic Ni-Cu-PGE sulfide ore deposits: Disseminated and net-textured ores: American Mineralogist, v. 102, p. 473–506.

Barnes, S.J., Holwell, D.A., and Le Vaillant, M., 2017b, Magmatic sulfide ore deposits: Elements, v. 13, p. 91–97.

Barnes, S.J., Stanley, C.R., and Taranovic, V., 2022, Compositions and Ni-Cu-PGE tenors of Nova-Bollinger ores with implications for the origin of Pt anomalies in PGE-poor massive sulfides: Economic Geology, v. 117, p. 1687-1707, doi: 10.5382/econgeo.4894.

Chai, G., and Naldrett, A.J., 1992a, The Jinchuan ultramafic intrusion: Cumulate of a high-Mg basaltic magma: Journal of Petrology, v. 33, p. 277–303.

——1992b, Characteristics of Ni-Cu-PGE mineralization and genesis of the Jinchuan deposit, Northwest China: Economic Geology, v. 87, p. 1475–1495.

Chai, G., Naldrett, A.J., Rucklidge, J.C., and Kilius, L.R., 1993, In-situ quantitative-analyses for PGE and Au in sulfide minerals of the Jinchuan Ni-Cu deposit by accelerator mass- spectrometry: The Canadian Mineralogist, v. 31, p. 19–30.

Chen, L.M., 2009, Features and genesis of segment I and its hosted Ni-Cu sulfide deposits of the Jinchuan intrusion, Gansu Province: Unpublished Ph.D. thesis, Guiyang, Graduate University of Chinese Academy of Sciences, 143 p. (in Chinese).

Chen, L.M., Song, X.Y., Keays, R.R., Tian, Y.L., Wang, Y.S., Deng, Y.F., and Xiao, J.F., 2013, Segregation and fractionation of magmatic Ni-Cu-PGE sulfides in the Western Jinchuan intrusion, northwestern China: Insights from platinum group element geochemistry: Economic Geology, v. 108, p. 1793–1811.

Chen, L.M., Song, X.Y., Danyushevsky, L.V., Wang, Y.S., Tian, Y.L., and Xiao, J.F., 2015, A laser ablation ICP-MS study of platinum-group and chalcophile elements in base metal sulfide minerals of the Jinchuan Ni-Cu sulfide deposit, NW China: Ore Geology Reviews, v. 65, p. 955–967.

Chung, H.Y., and Mungall, J.E., 2009, Physical constraints on the migration of immiscible fluids through partially molten silicates, with special

reference to magmatic sulfide ores: Earth and Planetary Science Letters, v. 286, no. 1–2, p. 4–22.
de Waal, S.A., Xu, Z.G., Li, C.S., and Mouri, H., 2004, Emplacement of viscous mushes in the Jinchuan ultramafic intrusion, western China: The Canadian Mineralogist, v. 42, p. 371–392.
Ding, X., Ripley, E.M., Underwood, B.S., Meng, Z.Y., and Huang, F., 2021, Behavior of Mg and C-O isotopes during mafic magma-carbonate interaction at the Jinchuan Ni-Cu deposit, North China craton: Chemical Geology, v. 562, p. 1–13.
Djon, M.L.N., and Barnes, S.J., 2012, Changes in sulfides and platinum-group minerals with the degree of alteration in the Roby, Twilight, and High Grade zones of the Lac des Iles Complex, Ontario, Canada: Mineralium Deposita, v. 47, p. 875–896.
Duan, J., Li, C., Qian, Z., Jiao, J., Ripley, E.M., and Feng, Y., 2016, Multiple S isotopes, zircon Hf isotopes, whole-rock Sr-Nd isotopes, and spatial variations of PGE tenors in the Jinchuan Ni-Cu-PGE deposit, NW China: Mineralium Deposita, v. 51, p. 557–574.
Eiler, J.M., 2001, Oxygen isotopic variations of basaltic lavas and upper mantle rocks: Reviews in Mineralogy and Geochemistry, v. 43, p. 320–364.
Godel, B., and Barnes, S.-J., 2008, Platinum-group elements in sulfide minerals and the whole rocks of the J-M reef (Stillwater Complex): Implication for the formation of the reef: Chemical Geology, v. 248, p. 272–294.
Godel, B., Barnes, S.-J., and Maier, W.D., 2007, Platinum-group elements in sulphide minerals, platinum-group minerals, and whole-rocks of the Merensky reef (Bushveld Complex, South Africa): Implications for the formation of the reef: Journal of Petrology, v. 48, p. 1569–1604.
González-Álvarez, I., Sweetapple, M., Lindley, I.D., and Kirakar, J., 2013, Hydrothermal Ni: Doriri Creek, Papua New Guinea: Ore Geology Reviews, v. 52, p. 37–57.
Helmy, H.M., Ballhaus, C., Wohlgemuth-Ueberwasser, C., Fonseca, R., and Laurenz, V., 2010, Partitioning of Se, As, Sb, Te and Bi between monosulfide solid solution and sulfide melt: Application to magmatic sulfide deposits: Geochimica et Cosmochimica Acta, v. 74, p. 6174–6179.
Holwell, D.A., Adeyemi, Z., Ward, L.A., Smith, D.J., Graham, S.D., McDonald, I., and Smith, J.W., 2017, Low temperature alteration of magmatic Ni-Cu-PGE sulfides as a source for hydrothermal Ni and PGE ores: A quantitative approach using automated mineralogy: Ore Geology Reviews, v. 91, p. 718–740.
Keays, R.R., and Jowitt, S.M., 2013, The Avebury Ni deposit, Tasmania: A case study of an unconventional nickel deposit: Ore Geology Reviews, v. 52, p. 4–17.
Keays, R.R., Nickel, E.H., Groves, D.I., and McGoldrick, P.J., 1982, Iridium and palladium as discriminants of volcanic-exhalative, hydrothermal, and magmatic nickel sulfide mineralization: Economic Geology, v. 77, p. 1535–1547.
Lehmann, J., Arndt, N.T., Windley, B., Zhou, M.F., Wang, C.Y., and Harris, C., 2007, Field relationships and geochemical constraints on the emplacement of the Jinchuan intrusion and its Ni-Cu-PGE sulfide deposit, Gansu, China: Economic Geology, v. 102, p. 75–94.
Le Vaillant, M.L., Barnes, S.J., Fiorentini, M.L., Miller, J., McCuaig, T.C., and Muccilli, P., 2015, A hydrothermal Ni-As-PGE geochemical halo around the Miitel komatiite-hosted nickel sulfide deposit, Yilgarn craton, Western Australia: Economic Geology, v. 110, p. 505–530.
Le Vaillant, M.L., Saleem, A., Barnes, S.J., Fiorentini, M.L., and Perring, J.M., 2016, Hydrothermal remobilisation around a deformed and remobilised komatiite-hosted Ni-Cu-(PGE) deposit, Sarah's Find, Agnew Wiluna greenstone belt, Yilgarn craton, Western Australia: Mineralium Deposita, v. 51, p. 369–388.
Li, C., and Naldrett, A.J., 1999, Geology and petrology of the Voisey's Bay intrusion: Reaction of olivine with sulfide and silicate liquids: Lithos, v. 47, p. 1–31.
Li, C., and Ripley, E.M., 2011, The giant Jinchuan Ni-Cu-(PGE) deposit: Tectonic setting, magma evolution, ore genesis and exploration implications: Reviews in Economic Geology, v. 17, p. 163–180.
Li, C., Xu, Z., Waal, S.A.D., Ripley, E.M., and Maier, W.D., 2004, Compositional variations of olivine from the Jinchuan Ni-Cu sulfide deposit, western China: Implications for ore genesis: Mineralium Deposita, v. 39, p. 159–172.
Li, C., Naldrett, A.J., and Ripley, E.M., 2007, Controls on the Fo and Ni contents of olivine in sulfide-bearing mafic/ultramafic intrusions: Principles, modeling, and examples from Voisey's Bay: Earth Science Frontiers, v. 14, p. 177–183.
Li, S.B., 2008, Magmatic evolution and the formation of Ni-Cu sulfide ore bodies in segment II of the Jinchuan intrusion, Gansu Province: Unpublished Ph.D. thesis, Guiyang, Graduate University of Chinese Academy of Sciences, 148 p. (in Chinese).
Mansur, E.T., Barnes, S.-J., and Duran, C.J., 2020, An overview of chalcophile element contents of pyrrhotite, pentlandite, chalcopyrite, and pyrite from magmatic Ni-Cu-PGE sulfide deposits: Mineralium Deposita, v. 1007, p. 126–156.
Mao, Y.J., Barnes, S.J., Duan, J., Qin, K.Z., Godel, B.M., and Jiao, J., 2018a, Morphology and particle size distribution of olivines and sulphides in the Jinchuan Ni-Cu sulphide deposit: Evidence for sulphide percolation in a crystal mush: Journal of Petrology, v. 59, p. 1701–1730.
Mao, Y.J., Qin, K.Z., Barnes, S.J., Ferraina, C., Iacono-Marziano, G., Verrall, M., Tang, D., and Xue, S., 2018b, A revised oxygen barometry in sulfide-saturated magmas and application to the Permian magmatic Ni-Cu deposits in the southern Central Asian orogenic belt: Mineralium Deposita, v. 53, p. 731–755.
Mungall, J.E., and Su, S., 2005, Interfacial tension between magmatic sulfide and silicate liquids: Constraints on the kinetics of sulfide liquation and sulfide migration through silicate rocks: Earth and Planetary Science Letters, v. 234, p. 135–149.
Mungall, J.E., Andrews, D.R.A., Cabri, L.J., Sylvester, P.J., and Tubrett, M., 2005, Partitioning of Cu, Ni, Au, and platinum-group elements between monosulfide solid solution and sulfide melt under controlled oxygen and sulfur fugacities: Geochimica et Cosmochimica Acta, v. 69, p. 4349–4360.
Mungall, J.E., Jenkins, M.C., Robb, S.J., Yao, Z., and Brenan, J.M., 2020, Upgrading of magmatic sulfides, revisited: Economic Geology, v. 115, p. 1827–1833.
Naldrett, A.J., 2004, Magmatic sulfide deposits—geology, geochemistry and exploration: Berlin, Heidelberg, New York, Springer, 727 p.
Naldrett, A.J., and Duke, J., 1980, Platinum metals magmatic sulfide ores: Science, v. 208, p. 1417–1424.
Pearce, T.H., 1968, A contribution to the theory of variation diagrams: Contributions to Mineralogy and Petrology, v. 19, p. 142–157.
Pirajno, F., and González-Álvarez, I., 2013, A re-appraisal of the Epoch nickel sulphide deposit, Filabusi greenstone belt, Zimbabwe: A hydrothermal nickel mineral system: Ore Geology Reviews, v. 52, p. 58–65.
Prichard, H.M., Knight, R.D., Fisher, P.C., McDonald, I., and Zhou, M.F., 2013, Distribution of platinum-group elements in magmatic and altered ores in the Jinchuan intrusion, China: An example of selenium remobilization by postmagmatic fluids: Mineralium Deposita, v. 48, p. 767–786.
Ripley, E.M., Sarkar, A., and Li, C., 2005, Mineralogic and stable isotope studies of hydrothermal alteration at the Jinchuan Ni-Cu deposit, China: Economic Geology, v. 100, p. 1349–1361.
Roeder, P.L., and Emslie, R.F., 1970, Olivine-liquid equilibrium: Contributions to Mineralogy and Petrology, v. 29, p. 275–289.
Sixth Geological Unit (SGU), 1984, Geology of the Baijiazuizi Cu-Ni sulfide deposit: Beijing Geological Survey of Gansu Province, Sixth Geological Unit, Geological Publishing House, 225 p. (in Chinese).
Song, X.Y., Zhou M.F., Wang, Y., Qi, L., and Zhang, C.J., 2006, Role of crustal contamination in formation of the Jinchuan intrusion and its world-class Ni-Cu-(PGE) sulfide deposit, Northwest China: International Geology Review, v. 48, p. 1113–1132.
Song, X.Y., Keays, R.R., Zhou, M.F., Qi, L., Ihlenfeld, C., and Xiao, J.F., 2009, Siderophile and chalcophile elemental constraints on the origin of the Jinchuan Ni-Cu-(PGE) sulfide deposit, NW China: Geochimica et Cosmochimica Acta, v. 73, p. 404–424.
Song, X.Y., Keays, R.R., Chen, L.M., Wang, Y.S., Tian, Y.L., and Xiao, J.F., 2012, Structural, lithological, and geochemical constraints on the dynamic magma plumbing system of the Jinchuan Ni-Cu sulfide deposit, NW China: Mineralium Deposita, v. 47, p. 277–297.
Su, S., Li, C., Zhou, M.F., Ripley, E.M., and Qi, L., 2008, Controls on variations of platinum-group element concentrations in the sulfide ores of the Jinchuan Ni-Cu deposit, western China: Mineralium Deposita, v. 43, p. 609–622.
Tang, Z.L., 1991, The metallogenetic model of the Jinchuan platinum-bearing copper-nickel sulphide deposit: International Symposium on Sulfide Deposits, Jinchang, Gansu, China, 1991, Proceedings, p. 17–43.
Tang, Z.L., and Li, W.Y., 1995, Mineralization model and geology of the Jinchuan deposit bearing PGE: Beijing, Geological Publishing House, 208 p. (in Chinese).
Tang, Z.L., Song, X.Y., and Su, S., 2009, Ni-Cu deposits related to high Mg basaltic magma, Jinchuan, western China, *in* Li, C., and Ripley, E.M., eds., New developments in magmatic Ni-Cu and PGE deposits: Beijing, Geological Publishing House, p. 121–140 (in Chinese).

Tonnelier, N.J., 2010, Geology and genesis of the Jinchuan Ni-Cu-(PGE) deposit, China: Unpublished Ph.D. thesis, Sudbury, Canada, Laurentian University, 214 p.

Valley, J.M., Lackey, J.S., Cavosie, A.J., Clechenko, C.C., Basei, M.S., Bindeman, I.N., Ferreira, V.P., Sial, A.N., King, E.M., Peck, W.H., Sinha, A.K., and Wei, C.S., 2005, 4.4 billion years of crustal maturation: Oxygen isotope ratios of magmatic zircon: Contributions to Mineralogy and Petrology, v. 150, p. 561–580.

Yang, S.H., Yang, G., Qu, W.J., Du, A.D., Hanski, E., Lahaye, Y., and Chen, J.F., 2017, Pt-Os isotopic constraints on the age of hydrothermal overprinting on the Jinchuan Ni-Cu-PGE deposit, China: Mineralium Deposita, v. 53, p. 757–774.

Yao, Z.S., Qin, K.Z., and Mungall, J.E., 2018, Tectonic controls on Ni and Cu contents of primary mantle-derived magmas for the formation of magmatic sulfide deposits: American Mineralogist, v. 103, p. 1545–1567.

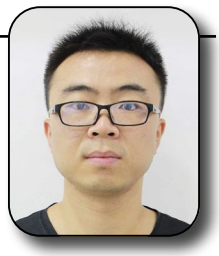

Jian Kang is a graduate student at the Institute of Geochemistry at the Chinese Academy of Sciences. He got a bachelor's degree from Kunming University of Science and Technology (China) in 2016. His Ph.D. degree research focuses on the chemical and physical formation mechanisms of the Jinchuan Ni-Cu-(PGE) deposit, Northwest China.

Xie-Yan Song is a geologist with particular interests in magmatic mineral deposits and related basaltic magmatism as well as PGE geochemistry. He joined the Institute of Geochemistry, Chinese Academy of Sciences, in Guiyang, China, in 2004 after Ph.D. study at The University of Hong Kong. He has published over 80 journal papers on the Ni-Cu-(PGE) sulfide deposits and the Fe-V-Ti magnetite deposits in the Emeishan large igneous province, North China craton, Central Asian orogenic belt, and East Kunlun orogenic belt, China.